TU Delft

Delft University of Technology

Extending the statistical linearization method to multi-variate non-differentiable nonlinearities in floating renewable energy devices

Tan, Jian; Zuo, Lei; Lavidas, George; Metrikine, Andrei

DOI
10.1016/j.renene.2025.123964

Publication date
2025

Document Version
Final published version

Published in
Renewable Energy

Citation (APA)
Tan, J., Zuo, L., Lavidas, G., & Metrikine, A. (2025). Extending the statistical linearization method to multi-variate non-differentiable nonlinearities in floating renewable energy devices. *Renewable Energy*, *256*, Article 123964. https://doi.org/10.1016/j.renene.2025.123964

Important note
To cite this publication, please use the final published version (if applicable).
Please check the document version above.

Copyright
Other than for strictly personal use, it is not permitted to download, forward or distribute the text or part of it, without the consent of the author(s) and/or copyright holder(s), unless the work is under an open content license such as Creative Commons.

Takedown policy
Please contact us and provide details if you believe this document breaches copyrights.
We will remove access to the work immediately and investigate your claim.

This work is downloaded from Delft University of Technology.
For technical reasons the number of authors shown on this cover page is limited to a maximum of 10.

Renewable Energy 256 (2026) 123964

Contents lists available at ScienceDirect

Renewable Energy

journal homepage: www.elsevier.com/locate/renene

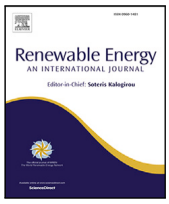

Extending the statistical linearization method to multi-variate non-differentiable nonlinearities in floating renewable energy devices

Jian Tan [a,*], Lei Zuo [b], George Lavidas [a], Andrei Metrikine [a]

[a] Faculty of Civil Engineering and Geosciences, Delft University of Technology, Stevinweg 1, 2628 CN, Delft, The Netherlands
[b] Department of Naval Architecture and Marine Engineering, University of Michigan, Ann Arbor, 48109, MI, USA

ARTICLE INFO

Keywords:
Non-differentiable nonlinearities
Statistical linearization
Floating renewable energy systems

ABSTRACT

This article investigates the methodology and applicability of the statistical linearization (SL) method to incorporating multi-variate non-differentiable nonlinearities, with a focus on floating renewable energy devices. The SL method serves as a highly competitive approach for analyzing floating renewable energy structures, such as wave energy converters (WECs) and floating wind energy turbines, because it inherently combines adequate accuracy and high computational efficiency. The origin of high accuracy comes from its incorporation of nonlinear effects through statistically linearized representations. Yet, the statistically linearized solutions have only been derived and verified for a limited number of nonlinearities of floating renewable energy devices, mostly simply-formed and differentiable in their mathematical expressions. However, floating renewable energy devices usually exhibit a complex dynamic mechanism, in which the relevant nonlinear effects could appear to be highly complex for linearization process to describe. These nonlinear effects could make a significant impact on the system dynamics, exemplified by external machinery force saturation and nonlinear hydrostatics of floaters with a non-uniform geometry. To push forward the boundary of the SL method, it is crucial to demonstrate how it applies to nonlinearities of different features.

In this paper, the existing SL method is extended to address the nonlinear effects expressed as multi-variate non-differentiable functions. Several case studies are carried out to exemplify the application of the extended SL approach to the concerned nonlinearities in floating renewable energy devices. The accuracy and computational efficiency of the extended SL approach are evaluated by verifying against the corresponding nonlinear time-domain (TD) and linear frequency-domain (FD) models. Despite the complexity of the given nonlinearities, the relative errors of the SL approach are no more than 6 % while its computational time is comparable to the FD model, being thousands of times faster than the TD model. Comparatively, the FD model leads to a relative error of over 70% in some cases.

1. Introduction

Ocean renewable energy holds immense potential towards the energy transition. These include offshore wind energy turbines, wave energy converters (WECs), ocean thermal energy plants and tidal turbines [1,2]. Over the past decades, ocean renewable energy sector has made significant achievements, marked by the increasing installation capacities [3]. In the pursuit of larger energy production, the sector has been heading to deeper water or larger support structures [4]. However, the ocean environmental complexity poses many challenges in further developing offshore renewable energy, especially the floating structures [5]. Hence, the sector has been continuing working hard to offer more reliable and robust designs of offshore renewable energy systems.

Numerical modeling has been widely recognized as a useful tool for advancing floating renewable energy systems, offering a resource- and time-efficient alternative to experimental and sea trial approaches [6]. It enables the analysis of dynamic behavior and power performance across various WEC designs, facilitating the characterization of design-performance relationships and driving iterative improvements towards cost-effective and efficient technologies. Common numerical modeling approaches include linear frequency-domain (FD), Cummins equation-based time-domain (TD), and Navier–Stokes equation-based Computational Fluid Dynamics (CFD) modeling [7]. CFD provides high-fidelity simulations of fully nonlinear phenomena but is computationally intensive, making it suitable for short-duration, extreme-condition simulations such as survivability examination [8]. The TD modeling approach, based on the Cummins equation [9], offers a balance between fidelity

* Corresponding author.
E-mail address: j.tan-2@tudelft.nl (J. Tan).

https://doi.org/10.1016/j.renene.2025.123964
Received 2 May 2025; Received in revised form 5 June 2025; Accepted 7 July 2025
Available online 15 July 2025
0960-1481/© 2025 The Authors. Published by Elsevier Ltd. This is an open access article under the CC BY license (http://creativecommons.org/licenses/by/4.0/).

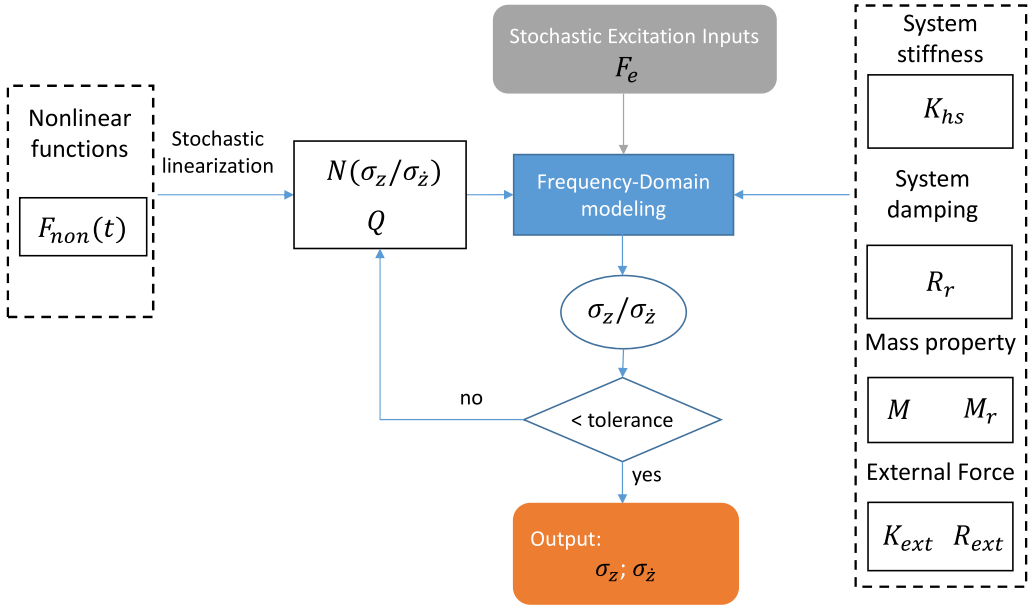

Fig. 1. Flowchart of implementing numerical simulation with using the SL method.

and efficiency by incorporating relevant nonlinear functions. In contrast, FD modeling relies on harmonic analysis, representing system responses as frequency-dependent components. Despite its high computational efficiency, the FD modeling is limited by its assumption of full linearity [10].

The computational efficiency of numerical models is crucial for the design and optimization of offshore renewable energy devices. These devices must withstand complex and ever-changing environmental conditions during their service. To ensure reliable and efficient designs, it is essential to accurately identify the loads and power production over a tremendous number of environmental inputs. For instance, the dynamic responses of floating devices are highly dependent on the properties of ocean waves, including wave heights and periods. As a result of the strong variability of ocean waves, the dynamics of the floating structures has to be estimated over a range of individual sea states to reveal the overall power performance or fatigue loads. The variability of ocean waves has two implications in the evaluation of the dynamics of floating energy devices. First, it is the long-term variability, which means the statistical characteristics of sea states are by no means constant. To describe the occurrence of numerous sea states of varied properties, the wave resource is normally characterized as a form of joint probability distribution of wave heights and periods based on long-term hind-cast statistics. Hence, to achieve a reasonable assessment, all the described sea states need to be addressed in the prediction of loads and power of floating renewable energy systems. The latter implies the short-term variability, in which each sea state needs to be represented by irregular waves. To reflect the randomness of irregular waves, the predefined wave train, in numerical simulation, is supposed to cover a sufficient time duration and consist of a wide range of wave frequency components [11]. As a consequence of these two factors, the computational-efficiency of numerical models is commonly highlighted in the simulation of offshore renewable energy systems.

Compared to TD modeling, FD modeling offers high computational efficiency but is limited to fully linear harmonic analysis. In contrast, the statistical linearization (SL) approach has emerged as a promising alternative in floating renewable energy systems, integrating high computational-efficiency with the ability to address nonlinear effects via linearized representations. Initial applications of the SL method to floating renewable energy systems focused on quadratic damping exerted on floaters and the excitation force decoupling in oscillating surge WECs [12], showing good agreement with nonlinear TD models in power capture and response spectra. Subsequent studies expanded the SL approach to include nonlinear effects such as damping [13], end-stop mechanisms [14], mooring stiffness [15], Coulomb damping [16,17], and machinery force capping [18]. Recent advancements [19,20] have further developed the SL approach to cover the nonlinearities across the full wave-to-wire process of WECs, incorporating both hydrodynamic and power conversion phases. More recently, the role of control tuning of WECs was investigated in [21], exemplifying the generalization of the SL method in floating renewable energy systems. The above-mentioned research has demonstrated the huge potential of the SL approach in estimating the dynamics of floating renewable energy systems. However, these works are predominantly limited to single-variate nonlinearities. The continued advancement of ocean renewable energy systems inevitably induces the demand of incorporating more realistic representations of complex mechanisms experienced by floating renewable energy devices. This inherently reflects the necessity of developing the SL approach to handle more complex nonlinear effects. Few studies have been recently conducted to account for multi-variate nonlinear functions by the SL method. For instance, in [17], the viscous drag term in the Morison equation was incorporated by the SL approach. However, as the Morison drag term depends on the difference between the wave velocity and the floater velocity, the linearization was accomplished by introducing an intermediate variable, namely the relative velocity between the two variables. Then, the linearization followed the procedures for the single-variate SL method. However, this exhibits limitations to complex multi-variate nonlinearities, in which multiple relative variables cannot be completely replaced by an intermediate variable. In [22], the SL approach was applied to address the bi-variate hydrostatic effect, in which the multi-variate stochastic linearization method was utilized. These pieces of initial work demonstrated the significance and feasibility of expanding the coverage of the SL method to multi-variate nonlinearities in floating renewable energy devices.

On the other hand, the differentiability could also distinguish the nonlinear functions into two types: differentiable nonlinearities and non-differentiable nonlinearities. Although the fundamental principle remains the same in the statistical linearization, the mathematical operation and derivation differ for addressing the differentiable nonlinearities and the non-differentiable nonlinearities. A widely applied equation, as systematically demonstrated in [23], to derive the linearized solution of a differentiable nonlinear term is: $K_{sl} = \mathbf{E}[\frac{\partial F_{non}(x)}{\partial x}]$.

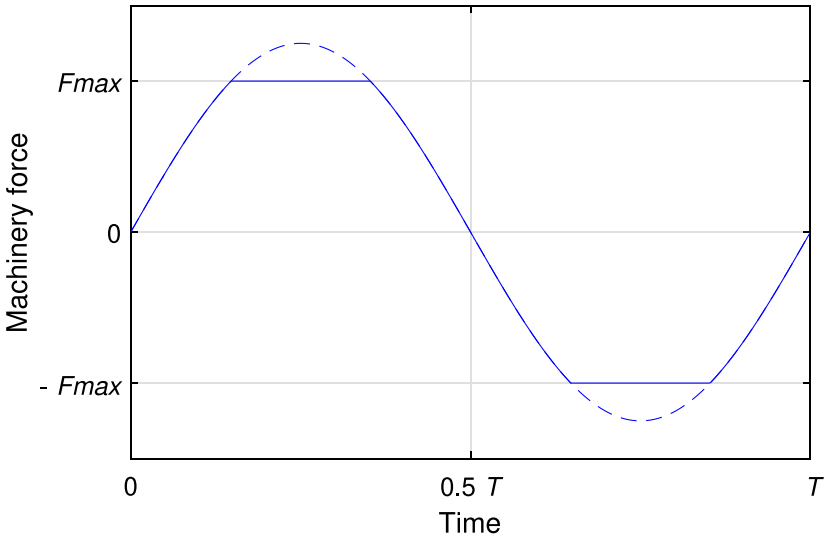

Fig. 2. Illustration of machinery force saturation.

K_{sl} is the statistically linearized coefficient, $F_{non}(x)$ is a nonlinear function of the variable x, and $\mathbf{E}(\cdot)$ denotes the expected value. This formulation has been widely adopted in recent studies to implement the SL procedure in numerical simulations. However, this equation is not applicable to non-differentiable nonlinear functions, which inherently restricts the SL approach from addressing a broader range of nonlinearities, as acknowledged in [12]. Hence, the existing SL method needs to be further developed to address the non-differentiability. In recent years, successful attempts were made to incorporate non-differentiable nonlinearities, such as Coulomb damping [14], external machinery force/torque saturation [18,19] by the SL approach. Nevertheless, these attempts are all limited to the single-variate nonlinear functions. Additionally, a recent study reported in [24] employed the formulation $K_{sl} = \mathbf{E}\left[\frac{\partial F_{non}(x)}{\partial x}\right]$ as described above, to address multivariate non-differentiable effects, namely power and torque saturation in WECs. The authors linearized the system by splitting the integration regions of different variables when addressing non-differentiable nonlinearities. This approach introduces a novel method for handling multivariate non-differentiable nonlinearities within the context of the SL method. However, the derivation process to arrive at this formulation fundamentally relies on the differentiability of the nonlinear functions. Therefore, the robustness of the method proposed in [24], which involves splitting the integration domain to ensure local differentiability and fit the form of the formulation $K_{sl} = \mathbf{E}\left[\frac{\partial F_{non}(x)}{\partial x}\right]$ requires further investigation. *Yet, the applicability of the SL approach to multi-variate non-differentiable nonlinearities has not been examined.* To push forward the boundary of the SL approach to a wider range, it is of huge significance to explore this aspect.

The present work is devoted to pushing forward the boundary of the SL approach to more complex nonlinear effects in modeling offshore renewable energy systems. Particularly, the extension moves towards the multi-variate non-differentiable nonlinearities. To achieve this primary goal, the mathematical derivation of the SL method is thoroughly revisited and modified to align with the addition of multi-variate non-differentiable nonlinearities. To generalize the derived solutions of the SL method, the discussion in this work expands from the existing widely-used SL method for single-variate differentiable nonlinearities to single-variate non-differentiable nonlinearities, then to multi-variate differentiable nonlinearities and finally up to multi-variate non-differentiable nonlinearities. For better applicability and clarity, the multi-variate non-differentiable nonlinearities are further classified into the type of correlated variables and uncorrelated variables to be discussed respectively. Subsequently, the three case studies in the offshore renewable energy systems are employed to verify the modified SL approach. The case studies start with the application of the SL method in handling multi-variate differentiable nonlinear effects. The Morison drag force on the cylindrical floating structure is demonstrated. The second case study exemplifies a non-differentiable nonlinear effect of multiple uncorrelated variables in WECs, namely PTO machinery force saturation with considering both the buoy velocity and displacement of the floater. In the second case, the nonlinear hydrostatic force exerted on a spar-buoy foundation with a non-uniform cross-sectional area is considered, representing the multi-variate non-differentiable nonlinear effects involving correlated variables. The reliability and computational efficiency of the extended SL approach are demonstrated in these case studies by being compared to the corresponding nonlinear TD model and linear FD model.

2. Overview of the statistical linearization approach

2.1. Equation of motion

The equation of motion is the foundation of building models for marine renewable energy devices. This subsection is intended to introduce the general form of the equation of motion when applying the SL method. To better distinguish the SL approach from other alternative approaches, the descriptions of the equation of motion in the TD modeling and the FD modeling are provided for comparison.

2.1.1. Nonlinear time-domain modeling

The equation of motion of floating structures is constructed based on the Cummins equation [9]:

$$[M+M_r(\infty)]\ddot{z}(t) = F_e(t)+F_{ext}(t)+F_{hs}(t)+F_{non}(t)+\int_{-\infty}^{t} K_{rad}(t-\tau)\dot{z}(\tau)d\tau \quad (1)$$

where

M: mass of the floating structure;

$M_r(\infty)$: added mass at the infinite frequency;

z, $\dot{z}$ and $\ddot{z}$: displacement, the velocity and the acceleration of the floater;

t: time;

F_e: wave excitation force;

F_{hs}: hydrostatic force;

F_{ext}: external force;

K_{rad}: radiation impulse function;

τ: intermediate variable used in the convolution;

F_{non}: a generic nonlinear correction term.

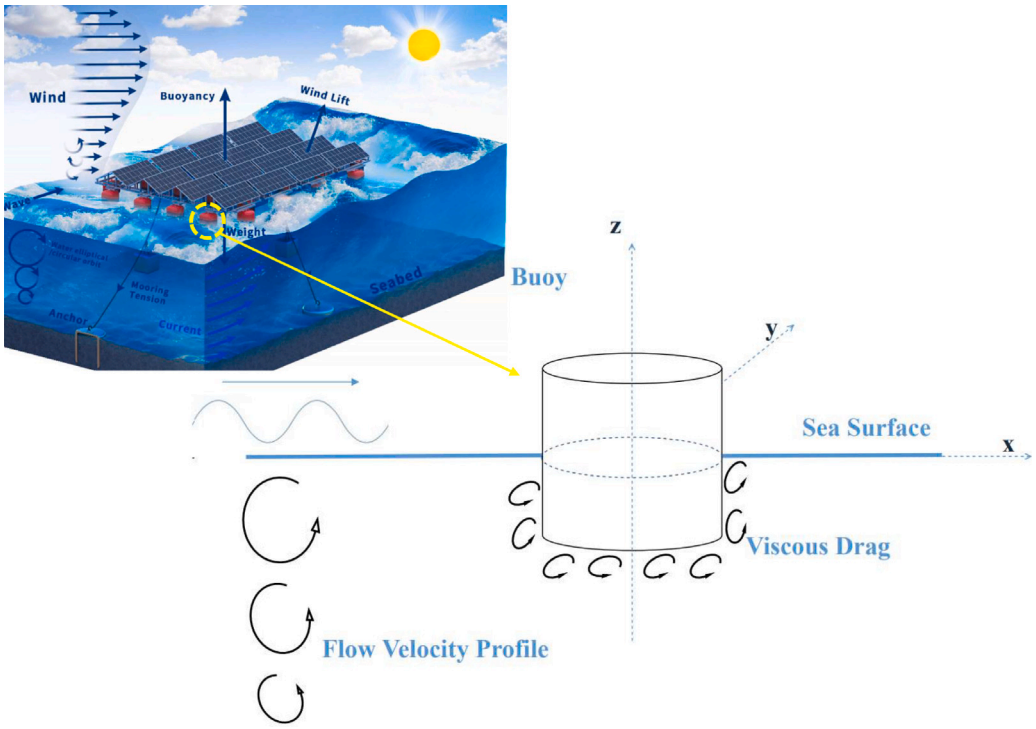

Fig. 3. Illustration of a floating cylindrical buoy with viscous drag effect [25].

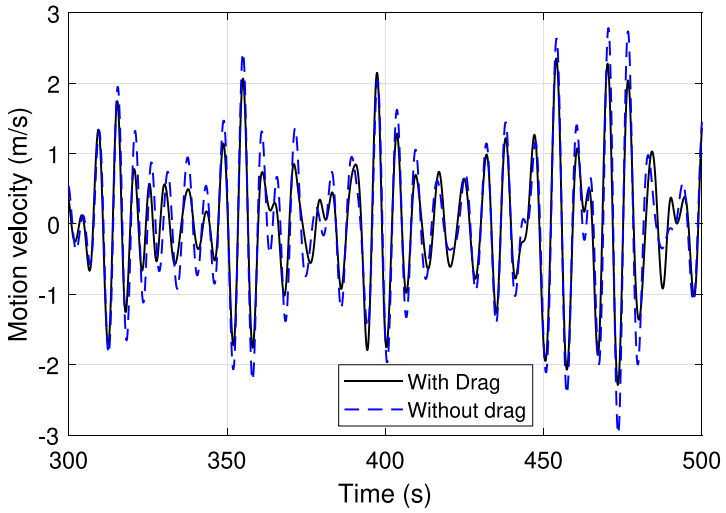

Fig. 4. Instantaneous motion velocity of the floater with and without considering the Morison drag force, $H_s = 3.0$ m and $T_p = 8.0$ s.

It should be noted that F_{non} is only intended to represent the weakly nonlinear hydrodynamic forces or external nonlinear forces which are added to the Cummins equation for corrections, while it cannot accurately describe highly nonlinear fluid–structure effects, such as vortex shedding. As the dynamics of a floater is deterministically computed at each time step, it is feasible to include the nonlinear component F_{non} in the process of the TD modeling.

2.1.2. Linear frequency-domain modeling

Assuming a linear system, the equation of motion of the floating structures can be described in the frequency domain as

$$\hat{F}_e(\omega) = \hat{z}(\omega)\left\{-\omega^2\left[M+M_r(\omega)\right]+K_{ext}(\omega)+K_{hs}+\mathrm{i}\omega\left[R_r(\omega)+R_{ext}(\omega)\right]\right\} \quad (2)$$

where

$\hat{F}_e$: complex amplitude of excitation force;

ω: angular frequency of the oscillation;

$\hat{z}$: complex amplitude of the displacement of the floater;

K_{ext}: external stiffness force coefficient;

K_{hs}: hydrostatic stiffness coefficient;

R_{ext}: external damping force coefficient;

R_r: radiation damping coefficient.

The conventional FD modeling approach is widely employed to estimate the dynamic behavior of linear systems. However, it is not inclusive to nonlinear components since it is built upon harmonic analysis. In this sense, there exists no nonlinear term in (2).

2.1.3. Statistical linearization approach

When applying the SL approach, the utilized equation of motion is built upon the framework of FD modeling. Comparatively, the contributions of nonlinear effects can be incorporated as additional terms into

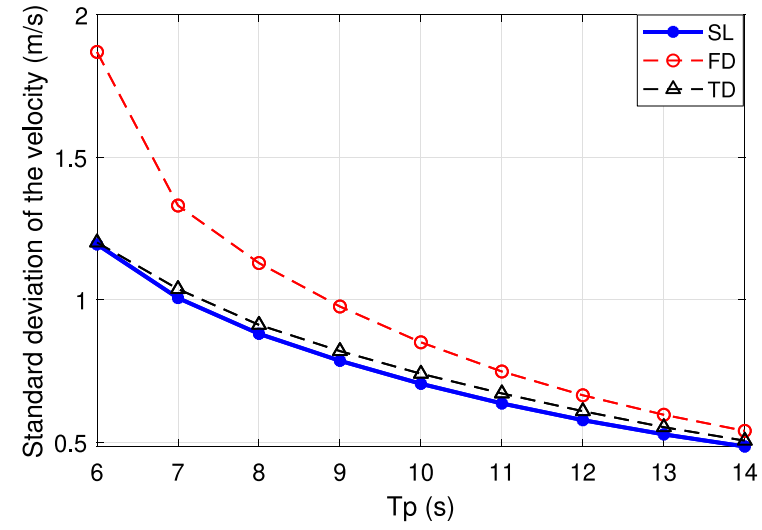

(a) Standard deviation of the floater velocity

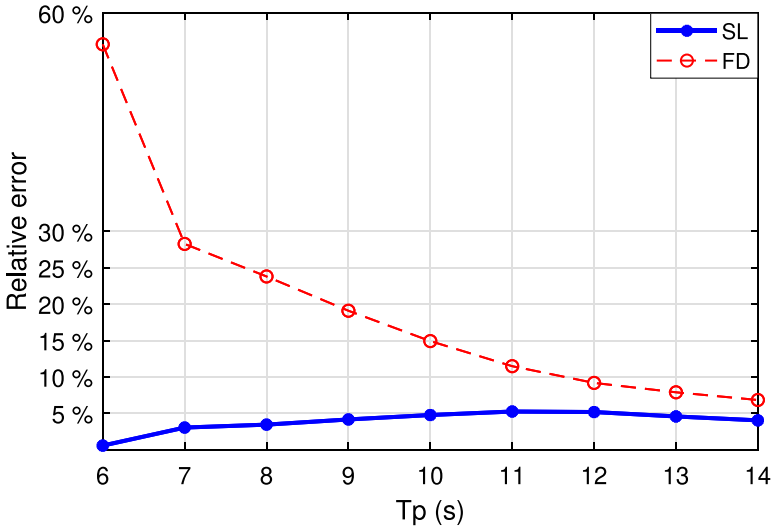

(b) The relative errors of the FD and SL approaches to the TD approach. The mean value of the standard deviation of the velocity across multiple TD simulation runs is used to calculate the relative errors.

Fig. 5. Comparison of standard deviation of the floater velocity predicted by different models along various peak period, $H_s = 3.0$ m.

the equation of motion as described in the frequency domain. These linearized terms are commonly derived using the SL method [23], which will be discussed in detail in Section 3.

$$\hat{F}_e(\omega) = \hat{z}(\omega)\Big\{-\omega^2\Big[M + M_r(\omega)\Big] + K_{ext}(\omega) + K_{hs} + K_{eq} + \mathrm{i}\omega\Big[R_r(\omega) + R_{ext}(\omega) + R_{eq}\Big]\Big\} \tag{3}$$

where

K_{eq}: linearized equivalent stiffness coefficient of the nonlinear forces;

R_{eq}: linearized equivalent damping coefficient of the nonlinear forces.

It should be noted that K_{eq} and R_{eq} are not frequency-dependent. They are related to the statistical estimates of the system responses in the frequency domain.

2.2. Workflow of the statistical linearization approach

The SL approach is regarded as an extension of the FD modeling approach. Specifically, when applying this approach, the equation of motion is constructed in the frequency domain, but nonlinear effects can be included by equivalent linear terms. The derivation of the equivalent linear terms is carried out based on the SL method. Given that the derived equivalent linear terms are inevitably related to the standard deviation of the responses σ_z or $\sigma_{\dot{z}}$ which are to be solved, it is necessary to implement an iterative process to find a solution to the equation of motion. The flowchart depicted in Fig. 1 exemplifies how to apply the SL method to solving dynamic responses of structures.

3. Mathematical derivation of statistical linearization

The mathematical derivation of SL for random vibration is presented in this section. The handling of various types of nonlinearities is discussed respectively. The discussion covers single-variate differentiable nonlinear functions, single-variate non-differentiable nonlinear functions, multi-variate differentiable nonlinear functions and multi-variate non-differentiable nonlinear functions. This part is intended to provide a comprehensive guideline of generalization of the SL method to complex multi-variate non-differentiable cases.

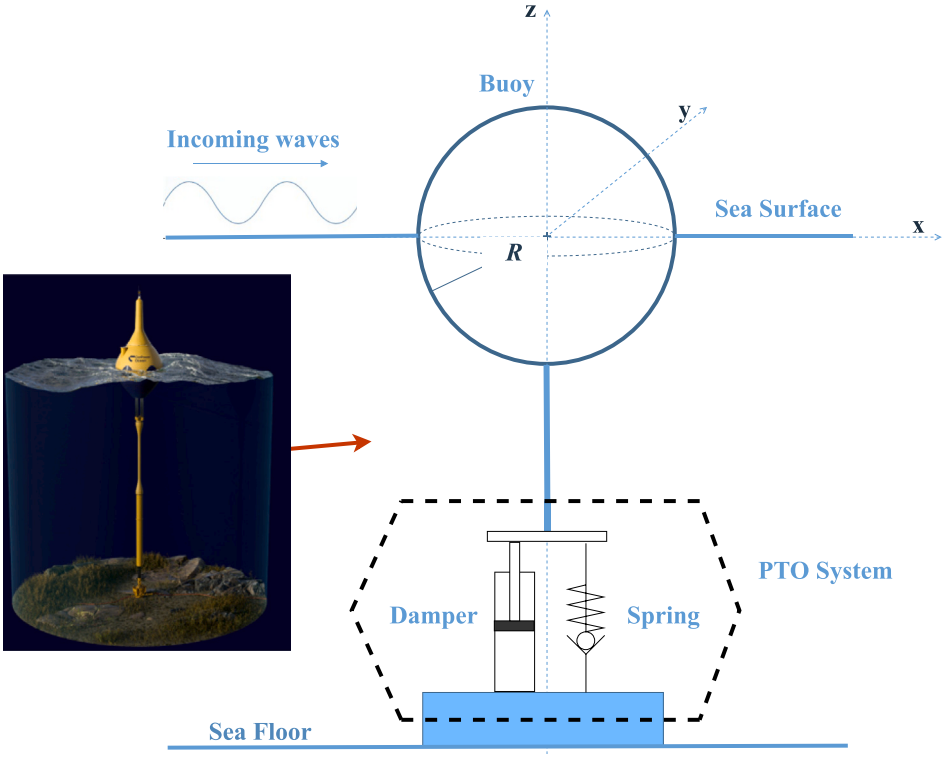

Fig. 6. Schematic of the spherical heaving point absorber with a bottom founded PTO system. Source by CorPower LTD.

3.1. Single-variate differentiable nonlinearities

Although the SL method for random vibration has been systematically demonstrated in [23], the applicability to non-differentiable nonlinearities, particularly multi-variate functions, has not been specifically demonstrated. A single-variate nonlinear function F_{non} can be expressed as

$$F_{non} = f(u) \tag{4}$$

where u is a zero-mean random variable and $f(u)$ embodies a general nonlinear function with respect to u. Let its linear approximation function, denoted as $f_{eq}(u)$, be expressed as

$$f_{eq}(u) = Nu + Q \tag{5}$$

here, N corresponds to the linearized coefficients which can be K_{eq} or R_{eq} in (3); Q is the mean part of the nonlinear function F_{non}. The resulting error in the linearization is given by

$$\epsilon = f(u) - Nu - Q \tag{6}$$

Statistically, the expected value of the error squared, denoted by $\mathbf{E}\left[\epsilon^2\right]$, is calculated as

$$\mathbf{E}\left(\epsilon^2\right) = \mathbf{E}\left[(f(u) - Nu - Q)^2\right] \tag{7}$$

where $\mathbf{E}(\cdot)$ denotes the expected value of a function. Minimizing the squared error requires N and Q to satisfy the following conditions:

$$\frac{\mathrm{d}}{\mathrm{d}N}\mathbf{E}\left(\epsilon^2\right) = 0 \quad \text{and} \quad \frac{\mathrm{d}}{\mathrm{d}Q}\mathbf{E}\left(\epsilon^2\right) = 0 \tag{8}$$

This gives

$$N = \frac{\mathbf{E}\left[uf(u)\right]}{\mathbf{E}\left(u^2\right)} \tag{9}$$

A property of a variable h following the Gaussian process can be expressed as

$$\mathbf{E}\left[f(h)h\right] = \mathbf{E}\left[h^2\right]\mathbf{E}\left[\frac{\mathrm{d}f(h)}{\mathrm{d}h}\right] \tag{10}$$

Therefore, the numerator in the right-hand side of (9) can be rewritten as

$$\mathbf{E}\left[uf(u)\right] = \mathbf{E}\left(u^2\right)\mathbf{E}\left[\frac{\mathrm{d}f(u)}{\mathrm{d}u}\right] \tag{11}$$

Then, combining (11) and (9) leads to

$$N = \mathbf{E}\left[\frac{\mathrm{d}f(u)}{\mathrm{d}u}\right] \tag{12}$$

where the expected value at the right-hand side of the equation can be calculated as

$$\mathbf{E}\left[\frac{\mathrm{d}f(u)}{\mathrm{d}u}\right] = \int_{-\infty}^{\infty}\frac{\mathrm{d}f(u)}{\mathrm{d}u}p(u)\mathrm{d}u \tag{13}$$

where $p(u)$ is the probability density function of the variable u. Assuming that the variable u follows Gaussian distribution, the probability density function is then expressed as

$$p(u) = \frac{1}{\sigma_u\sqrt{2\pi}}\exp(-\frac{u^2}{2\sigma_u^2}) \tag{14}$$

where σ_u is the standard deviation of the variable u.

To derive the mean-part contribution Q, $\frac{\mathrm{d}}{\mathrm{d}Q}\mathbf{E}\left(\epsilon^2\right)$ is expanded as follows

$$\begin{aligned}\frac{\mathrm{d}}{\mathrm{d}Q}\mathbf{E}\left(\epsilon^2\right) &= E\left\{\frac{\mathrm{d}}{\mathrm{d}Q}\left[f(\mathbf{u}(t)) - Nu(t) - Q\right]^2\right\} \\ &= \mathbf{E}\left\{2\left[-f(u(t)) + Nu(t) + Q\right]\right\} \\ &= -2\mathbf{E}[f(u(t))] + 2\mathbf{E}\left[Nu(t)\right] + 2\mathbf{E}[Q]\end{aligned} \tag{15}$$

It is noted that N and Q are scalar for single-variate linearization cases, while they will be expressed in the form of vectors in the later extension for multi-variate linearization applications. As the variable u adheres to a zero-mean Gaussian distribution, (15) can be rewritten as

$$\begin{aligned}\frac{\mathrm{d}}{\mathrm{d}Q}\mathbf{E}\left(\epsilon^2\right) &= -2\mathbf{E}[f(\mathbf{u}(t))] + 2Q \\ &= 2\{Q - \mathbf{E}[f(\mathbf{u}(t))]\}\end{aligned} \tag{16}$$

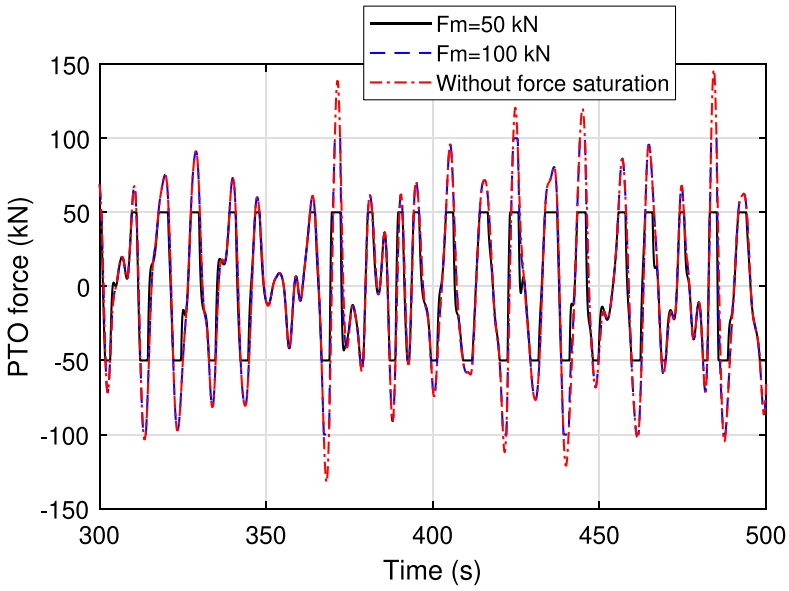

(a) Instantaneous PTO force.

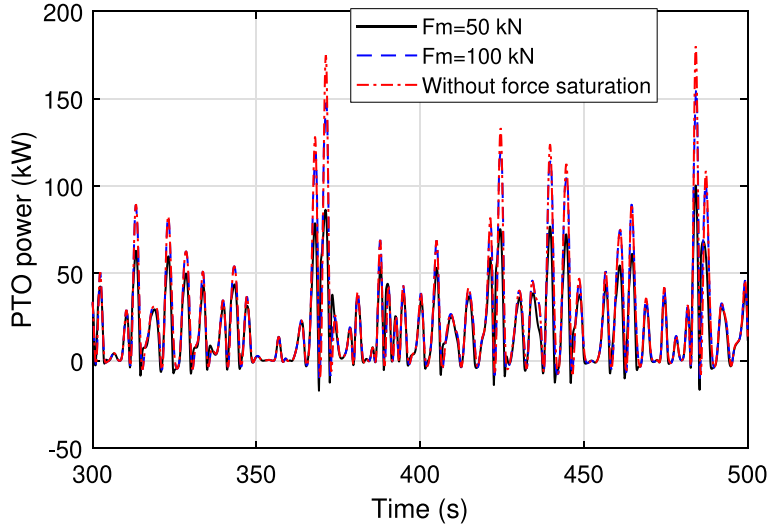

(b) Instantaneous PTO power

Fig. 7. Instantaneous PTO force and PTO power of the WEC with different PTO force limits. The simulation conditions are $H_s = 4$ m; $T_p = 10$ s; $B_{pto} = 100$ kNs/m and $K_{pto} = 40$ kN/m.

As depicted in (8), to satisfy $\frac{\mathrm{d}}{\mathrm{d}Q}\mathbf{E}\left(\epsilon^2\right) = 0$, Q can therefore be calculated as

$$Q = \mathbf{E}[f(u(t))] \tag{17}$$

where the expected value can be further derived, given the Gaussian process, as

$$\begin{aligned} Q &= \mathbf{E}[f(u(t))] \\ &= \int_{-\infty}^{\infty} f(u)p(u)\mathrm{d}u \end{aligned} \tag{18}$$

3.2. Single-variate non-differentiable nonlinearities

The principle of SL for non-differentiable functions remains identical, that is to minimize the relative error shown in (7). However, the non-differentiability of the function would violate the property expressed in (10). In this sense, the linearized solution has to be derived following (9) rather than (12).

A typical non-differentiable case is the machinery force saturation. The illustration of machinery force saturation is as depicted in Fig. 2. A short elaboration with regard to the linearization of machinery force saturation is given below. The expected energy dissipation of a force saturation function F_{sa} is given as

$$\begin{aligned} J &= \mathbf{E}(F_{sa}u) \\ &= \mathbf{E}[(F_{unconstrained} + F_{constrained})u] \\ &= \mathbf{E}[F_{unconstrained}u] + \mathbf{E}[F_{constrained}u] \end{aligned} \tag{19}$$

If (12) is by mistake applied to non-differentiable nonlinear functions, the derivative of the saturated part of the function $F_{constrained}$ in (19) would be simply zero. As mentioned, the linearized solution is expected to make the same energy or power dissipation. However, in this way, the contribution of the saturated part would be dismissed, which inevitably leads to inaccuracy in the linearized solutions. Other similar nonlinear effects can refer to the end-stop mechanism and Coulomb damping in wave energy conversion [26].

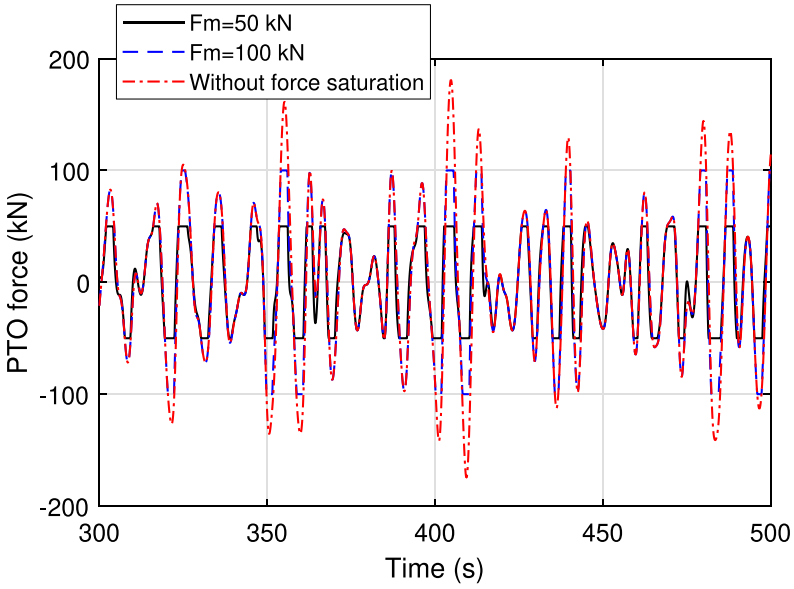

(a) Instantaneous PTO force.

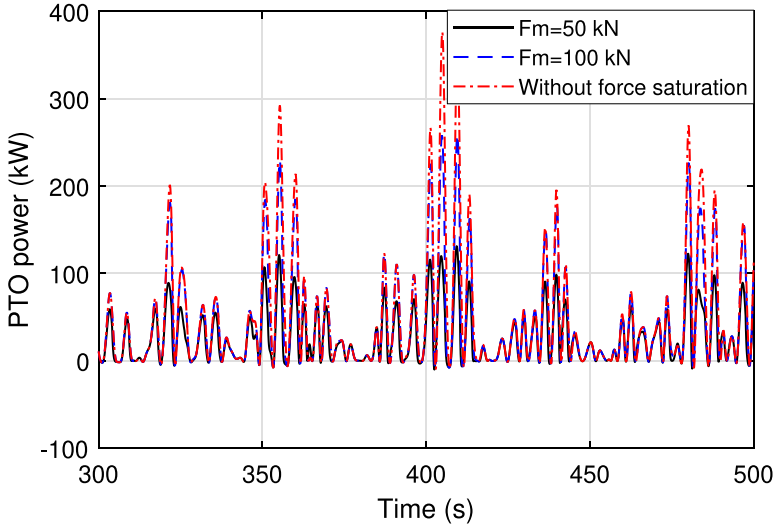

(b) Instantaneous PTO power

Fig. 8. Instantaneous PTO force and PTO power of the WEC with different PTO force limits. The simulation conditions are $H_s = 4$ m; $T_p = 10$ s; $B_{pto} = 80$ kNs/m and $K_{pto} = -20$ kN/m.

3.3. Multi-variate differentiable nonlinearities

The SL approach for multivariate nonlinearities, as derived in [27], assumes that the nonlinear effects are inherently non-differentiable. For context, a brief overview of the derivation is provided below.

A nonlinear function F_{non} of n variables can be expressed in a generic form as

$$F_{non} = f(u_1, u_2, \dots, u_n) \tag{20}$$

in which $f(\cdot)$ stands for a nonlinear function; and $u_1(t), u_2, \dots, u_n(t)$ represent the random zero-mean input variables to the function. The variables can be expressed in the form of a vector as $\mathbf{u}(t) = [u_1(t) \;\; u_2(t) \;\; \cdots \;\; u_n]^{\mathrm{T}}$. statistical linearization could give an approximation to the nonlinear function as

$$F_{non}(\mathbf{u}) \approx \mathbf{N}\mathbf{u} + Q \tag{21}$$

where $\mathbf{N}$ represents the vector of the linearized coefficients, and $\mathbf{N} = [N_1 \;\; N_2 \;\; \cdots \;\; N_n]$, and Q is a constant corresponding to the mean part of the nonlinear function. In this sense, the squared error of the linearized solution is expressed as

$$\epsilon(\mathbf{N}, Q) = \mathbf{E}\left\{\left[f(\mathbf{u}(t)) - \mathbf{N}^{\mathrm{T}}\mathbf{u}(t) - Q\right]^2\right\} \tag{22}$$

To minimize the squared error, the vector of the linearized coefficients should satisfy

$$\frac{\partial \epsilon(\mathbf{N}, Q)}{\partial \mathbf{N}} = 0 \tag{23}$$

(23) can be further derived as

$$\begin{aligned}\frac{\partial \epsilon(\mathbf{N}, Q)}{\partial \mathbf{N}} &= \begin{bmatrix} \frac{\partial \epsilon(\mathbf{N},Q)}{\partial N_1} \\ \frac{\partial \epsilon(\mathbf{N},Q)}{\partial N_2} \\ \vdots \\ \frac{\partial \epsilon(\mathbf{N},Q)}{\partial N_n} \end{bmatrix} \\ &= -2\mathbf{E}\left(\begin{bmatrix} u_1(t) f(\mathbf{u}(t)) \\ u_2(t) f(\mathbf{u}(t)) \\ \vdots \\ u_n(t) f(\mathbf{u}(t)) \end{bmatrix}\right) + 2\mathbf{cov}\left[\mathbf{u}(t)\right]\begin{bmatrix} N_1 \\ N_2 \\ \vdots \\ N_n \end{bmatrix}\end{aligned} \tag{24}$$

where $\mathbf{cov}[\mathbf{u}(t)]$ represents the covariance of vector $\mathbf{u}(t)$.

For multi-variate input vector $\mathbf{H}$ following the Gaussian process, the property described in (10) can be extended as

$$\mathbf{E}[f(\mathbf{H})\mathbf{H}] = \mathbf{E}\left[\mathbf{H}\mathbf{H}^T\right]\mathbf{E}[\nabla f(\mathbf{H})] \tag{25}$$

where $\boldsymbol{\nabla}$ means the gradient operator, and it is given as

$$\boldsymbol{\nabla} = \left[\frac{\partial}{\partial H_1}, \frac{\partial}{\partial H_2}, \cdots, \frac{\partial}{\partial H_n}\right]^{\mathrm{T}} \tag{26}$$

Besides, the covariance matrix of the input variables is calculated as

$$\mathbf{cov}[\mathbf{u}(t)] = \mathbf{E}\left\{\mathbf{u}(t)\mathbf{u}(t)^{\mathbf{T}}\right\} \tag{27}$$

Then, applying (25) and (27) to (24) gives

$$\begin{aligned}\frac{\partial \epsilon(\mathbf{N}, Q)}{\partial \mathbf{N}} &= -2\mathbf{E}\left\{\mathbf{u}(t)\mathbf{u}^{\mathbf{T}(t)}\right\} E\left\{\boldsymbol{\nabla} f(\mathbf{u}(t))\right\} + 2\mathbf{cov}[\mathbf{u}(t)]\mathbf{N} \\ &= 2\mathbf{cov}[\mathbf{u}(t)]\left\{\mathbf{N} - \mathbf{E}[\boldsymbol{\nabla} f(\mathbf{u}(t))]\right\}\end{aligned} \tag{28}$$

Let $\frac{\partial \epsilon(\mathbf{N},Q)}{\partial \mathbf{N}} = 0$, the vector of the linearized coefficients can be given as

$$\mathbf{N} = \mathbf{E}[\boldsymbol{\nabla} f(\mathbf{u}(t))] \tag{29}$$

where the calculation of the i_{th} element of the expected value in (29) can be done as

$$\begin{aligned}N_i &= \mathbf{E}[\frac{\partial f(\mathbf{u})}{\partial u_i}] \\ &= \int_{-\infty}^{\infty}\int_{-\infty}^{\infty}\cdots\int_{-\infty}^{\infty}\frac{\partial f(\mathbf{u})}{\partial u_i} p(\mathbf{u})\, du_n \cdots du_2\, du_1\end{aligned} \tag{30}$$

where $p(\mathbf{u})$ denotes the multivariate probability density function. As the vector $\mathbf{u}$ is zero-mean and adheres to the multivariate Gaussian distribution, the multivariate probability density function can be expressed as

$$p(\mathbf{u}) = \frac{1}{(2\pi)^{n/2}|\mathbf{cov}(\mathbf{u})|^{1/2}} \exp\left(-\frac{1}{2}\mathbf{u}^{\mathrm{T}}[\mathbf{cov}(\mathbf{u}(t))]^{-1}\mathbf{u}\right) \tag{31}$$

where $|\mathbf{cov}(\mathbf{u})|$ and $[\mathbf{cov}(\mathbf{u}(t))]^{-1}$ represents the determinant and the inverse of the covariance matrix.

3.4. Multi-variate non-differentiable nonlinearities

3.4.1. Correlated input variables

The property of Gaussian variables which is described as in (25) is not applicable to multi-variate non-differentiable functions. In this sense, let (24) to be zero gives

$$\frac{\partial \epsilon(\mathbf{N}, Q)}{\partial \mathbf{N}} = -2\mathbf{E}\left(\begin{bmatrix} u_1(t)f(\mathbf{u}(t)) \\ u_2(t)f(\mathbf{u}(t)) \\ \vdots \\ u_n(t)f(\mathbf{u}(t)) \end{bmatrix}\right) + 2\mathbf{cov}[\mathbf{u}(t)]\begin{bmatrix} N_1 \\ N_2 \\ \vdots \\ N_n \end{bmatrix} = 0 \tag{32}$$

Therefore, the vector of linearized coefficients $\mathbf{N}$ can be derived as

$$\mathbf{N} = [\mathbf{cov}(\mathbf{u}(t))]^{-1}\mathbf{E}\left(\begin{bmatrix} u_1(t)f(\mathbf{u}(t)) \\ u_2(t)f(\mathbf{u}(t)) \\ \vdots \\ u_n(t)f(\mathbf{u}(t)) \end{bmatrix}\right) \tag{33}$$

The covariance matrix is expressed as

$$\mathbf{cov}(\mathbf{u}(t)) = \begin{bmatrix} \sigma_{u_1}^2 & \sigma_{u_1u_2} & \cdots & \sigma_{u_1u_n} \\ \sigma_{u_2u_1} & \sigma_{u_2}^2 & \cdots & \sigma_{u_2u_n} \\ \vdots & \vdots & \ddots & \vdots \\ \sigma_{u_nu_1} & \sigma_{u_nu_2} & \cdots & \sigma_{u_n}^2 \end{bmatrix} \tag{34}$$

where diagonal terms represent the variances of the variables, and the expected values in (33) can be derived as

$$\mathbf{E}[u_i f(\mathbf{u})] = \int_{-\infty}^{\infty}\int_{-\infty}^{\infty}\cdots\int_{-\infty}^{\infty} u_i f(\mathbf{u}) p(\mathbf{u})\, du_n \cdots du_2\, du_1 \tag{35}$$

3.4.2. Uncorrelated input variables

In particular cases, the input variables are uncorrelated. Then, all the off-diagonal terms appear to be zero on the covariance matrix. Hence, the inverse of the covariance matrix can be expressed as

$$[\mathbf{cov}(\mathbf{u}(t))]^{-1} = \begin{bmatrix} \frac{1}{\sigma_{u_1}^2} & 0 & \cdots & 0 \\ 0 & \frac{1}{\sigma_{u_2}^2} & \cdots & 0 \\ \vdots & \vdots & \ddots & \vdots \\ 0 & 0 & \cdots & \frac{1}{\sigma_{u_n}^2} \end{bmatrix} \tag{36}$$

Substituting (36) into (37) gives the solution of the vector of the linearized coefficients:

$$\mathbf{N} = \begin{pmatrix} \frac{\mathbf{E}[u_1(t)f(\mathbf{u}(t))]}{\sigma_{u_1}^2} \\ \frac{\mathbf{E}[u_2(t)f(\mathbf{u}(t))]}{\sigma_{u_2}^2} \\ \vdots \\ \frac{\mathbf{E}[u_n(t)f(\mathbf{u}(t))]}{\sigma_{u_n}^2} \end{pmatrix} \tag{37}$$

4. Case studies

The application of the SL approach to single-variate nonlinearities have been thoroughly demonstrated in previous work. These nonlinearities include quartic damping terms, second-order stiffness, cosine function, etc. More details can be referred to the work reviewed in Introduction of this work. In this sense, the following case studies are only aiming to exemplify the application of the SL method to incorporating more complex nonlinearities in floating renewable energy devices. This work presents three case studies involving both multivariate differentiable and non-differentiable nonlinearities. Case Study 1 focuses on the Morison drag term, a widely used formulation in offshore engineering for considering viscous effects. Although the Morison drag term is inherently a multivariate differentiable function, it is included here to provide a basis for comparison with that used to handle non-differentiable nonlinearities. In the context of multivariate non-differentiable nonlinearities, two distinct examples are presented to illustrate cases involving uncorrelated and correlated variables. Case Study 2 examines the saturation of the PTO force in WECs under reactive control, representing a non-differentiable function of uncorrelated variables. Case Study 3 addresses the nonlinear hydrostatic forces acting on a non-uniform spar buoy, exemplifying a non-differentiable function of correlated variables. Furthermore, it is important to acknowledge that additional complex nonlinear effects exist in floating renewable energy systems beyond those addressed in the three case studies presented. Notable examples include the combined power and force saturation in WECs [24], nonlinear mooring dynamics [29], and nonlinear aerodynamic effects in floating wind turbines [30]. Therefore, the application of the extended SL method to these examples merits further investigation in future research.

The hydrodynamic coefficients of all floating structures involved in the following case studies are numerically computed using the open-source Boundary Element Method (BEM) solver Nemoh [31]. The linear wave theory is considered throughout all the case studies, and the JONSWAP spectrum is employed to describe the irregular wave conditions [32] in all simulation approaches presented in this work. Each irregular wave train is generated by the superposition of 1000 individual harmonic wave components with random phases. In the SL approach, the calculation of statistically-linearized coefficients requires the derivation of the mathematical exception of the nonlinear functions. The closed-form solution is difficult to be explicitly expressed given the multi-layer integral in multivariate cases, as (30) and (35). Hence, the integral is derived using the numerical integration scheme in this study. As the linearized coefficients are related to standard deviations of the responses which are to be solved, an iterative solver is needed in the SL approach as discussed earlier. Throughout all the simulation cases

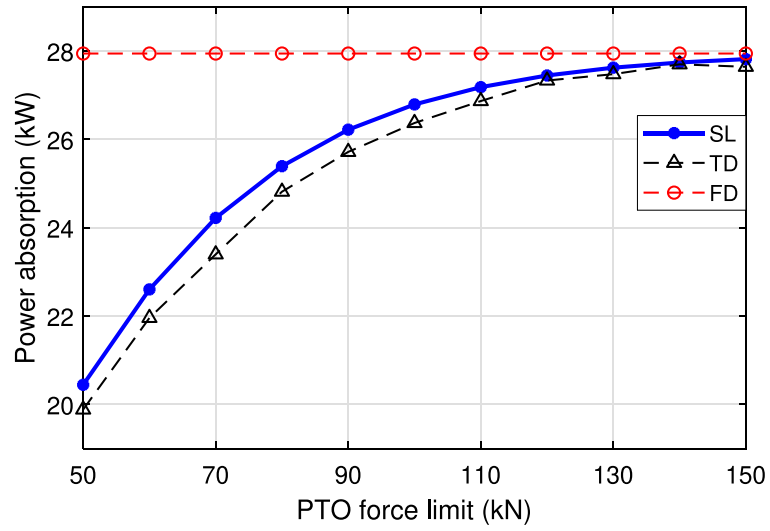

(a) The absorbed power of WEC.

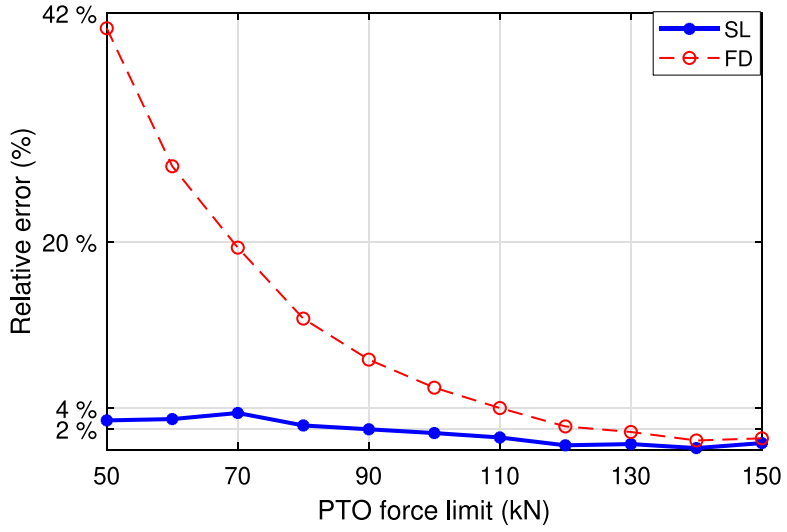

(b) The relative errors of the FD and SL approach to the TD approach. The mean value of the power absorption across multiple TD simulation runs is used to calculate the relative errors.

Fig. 9. Comparison of the power absorption of the WEC predicted by different models along various PTO force limits. The simulation conditions are $H_s = 4$ m; $T_p = 10$ s; $B_{pto} = 100$ kNs/m and $K_{pto} = 40$ kN/m.

in this study, the convergence criterion for the iterative solution of the standard deviation of the unknown dynamic responses is consistently set to 0.01% [13,16]. The derived linearized coefficients can be referred to Appendix.

For all the case studies, the corresponding nonlinear TD model and linear FD model are also executed to provide comparative results. The TD model is considered the reference solution due to its higher fidelity. It is formulated based on Cummins' equation, as shown in (1), where the convolution term is approximated using a state-space representation following the approach described in [33], for the sake of reducing computational burden. The ODE45 solver in the MATLAB environment is used to derive the differential equation in the TD model, with a time step set to 0.01 times the peak period of the considered sea state. For a specific sea state, the peak period is defined as the wave period of the most energetic waves in a sea state [26]. To minimize random errors, each TD simulation is repeated 30 times, with different random phase sets assigned to the harmonic wave components for each irregular wave train. The simulation duration is defined as 125 times the peak period of the considered sea state. The initial 25 peak periods serve as a ramp time to mitigate strong system transients at the start of the simulation [11]; however, this ramp period is excluded from the post-processed results of the TD model.

4.1. Multi-variate differentiable nonlinearity: Morison drag force (case study 1)

The viscous drag force has a significant influence on the dynamics of floating structures [34]. Incorporating the drag effect into the assessment of floating support structures can improve the understanding of the power performance and load conditions of marine renewable energy systems. As commonly used floating foundations, cylinder-type buoys have been applied in various applications, such as floating photovoltaic (PV) systems [25] and floating wind turbines [35]. Therefore, the current case study is dedicated to modeling of the viscous drag effect on a heaving cylindrical buoy, as illustrated in Fig. 3.

The Morison equation is widely utilized to estimate the viscous drag force exerted on floating structures [32]. The study of using the SL method in to address Morison equation has been performed in previous

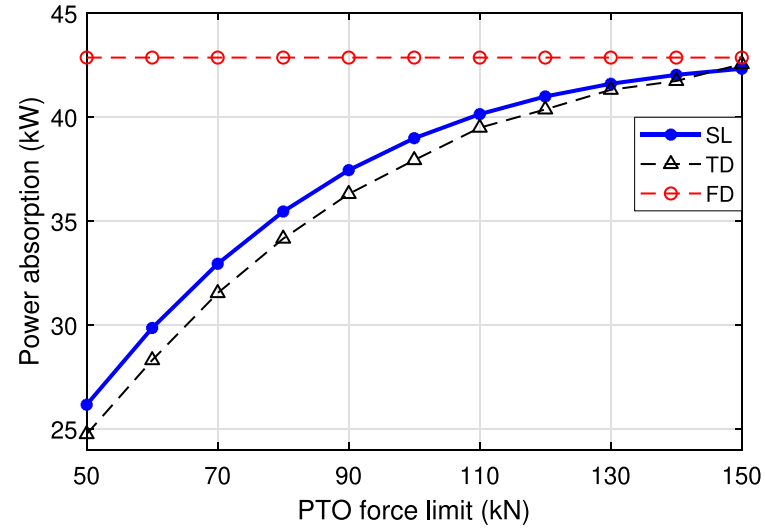

(a) The absorbed power of WEC.

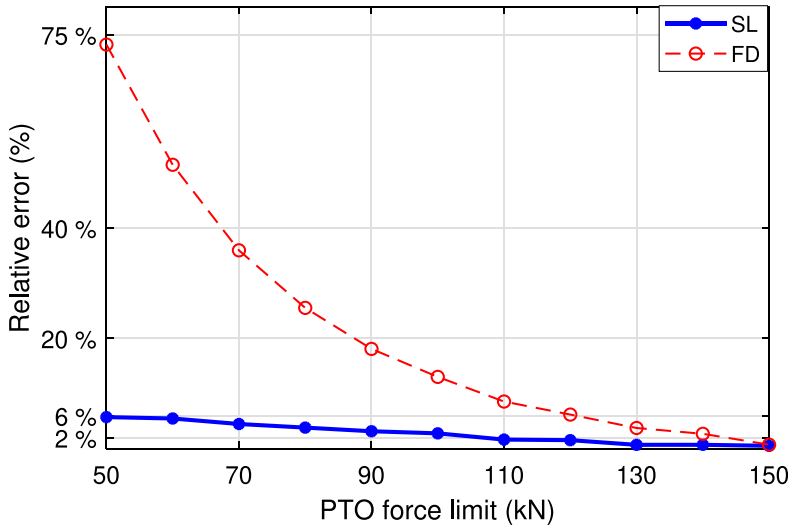

(b) The relative errors of the FD and SL approaches to the TD approach. The mean value of the power absorption across multiple TD simulation runs is used to calculate the relative errors.

Fig. 10. Comparison of the power absorption of the WEC predicted by different models along various PTO force limits. The simulation conditions are $H_s = 4$ m; $T_p = 10$ s; $B_{pto} = 80$ kNs/m and $K_{pto} = -20$ kN/m.

work [12] to incorporate nonlinear drag force. However, to ease the linearization procedure, the multi-variate function was simplified to be a single-variate case where the term was assumed to be only related to fluid velocity or structure velocity. Only recently in [17], the influence of the wave field and the floater motion was both considered in the SL approach by introducing a relative variable, which highlighted the importance of including both variables. In the current case study, a more general and straightforward approach, namely the multi-variate linearization method, within the SL framework. In this method, the introduction of a relative variable is not required.

Based on the Morison equation, the viscous drag force is expressed as

$$F_{vis} = -\frac{1}{2} C_d \rho A_s (v_b - v_w)|(v_b - v_w)| \tag{38}$$

where F_{vis} is the viscous drag force; C_d is the drag coefficient; A_s is the area of the body projected to the moving direction; ρ is the water density; v_b and v_w are the body velocity and the wave velocity respectively. In the frequency domain, the linearized representation of the Morison term can be given as

$$\hat{F}_{vis}(\omega) = R_{eq,b}\hat{v}_b(\omega) + R_{eq,w}\hat{v}_w(\omega) \tag{39}$$

where $\hat{v}_b$ and $\hat{v}_w$ are the complex amplitude of the buoy velocity and the wave velocity respectively; $R_{eq,b}$ and $R_{eq,w}$ are the statistically linearized viscous damping coefficients of the buoy velocity and the wave velocity. Besides, it is noted that the function (38) is differentiable to both variables, v_b and v_w. Then, following (29), the vector of the linearized coefficients can be obtained as

$$\begin{bmatrix} R_{eq,b} \\ R_{eq,w} \end{bmatrix} = \mathbf{E}\left(\begin{bmatrix} \frac{\partial F_{vis}(v_b, v_w)}{\partial v_b} \\ \frac{\partial F_{vis}(v_b, v_w)}{\partial v_w} \end{bmatrix} \right) \tag{40}$$

Thus, the equation of motion of the SL approach can be rewritten as

$$\hat{F}_{e,cy}(\omega) - R_{eq,w}\hat{v}_w(\omega) = \hat{z}_b(\omega)\Big\{ -\omega^2 \Big[M_{cy} + M_{r,cy}(\omega) \Big] + K_{hs,cy} + \mathrm{i}\omega \Big[R_{r,cy}(\omega) + R_{eq,b} \Big] \Big\} \tag{41}$$

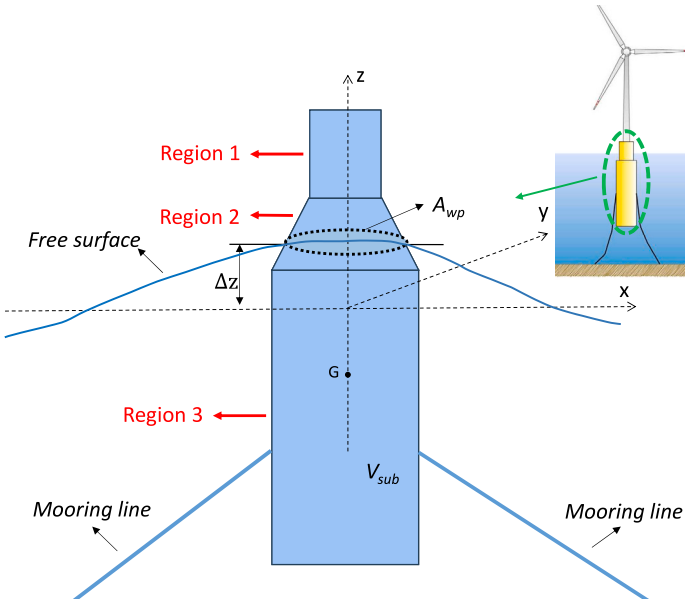

(a) Illustration of the exact position of the spar buoy with considering the instantaneous free surface [47]

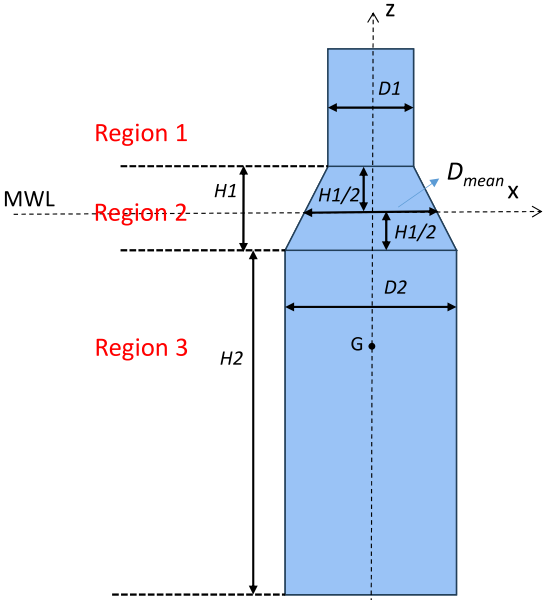

(b) The geometrical drawing of the spar buoy

Fig. 11. The representation of the exact buoyancy force of a spar buoy with a non-uniform cross-sectional area. 'MWL' embodies the mean water level [28].

where $\hat{z}_b$ is the complex amplitude of the buoy displacement; $F_{e,cy}$ stands for the excitation force of the cylindrical buoy; M_{cy} and $M_{r,cy}$ are the mass and the added mass of the buoy; $K_{hs,cy}$ embodies the linear hydrostatic coefficient of the buoy; and $R_{r,cy}$ denotes the radiation damping of the cylindrical buoy. Note that K_{ext} and R_{ext} are dismissed from the general form of the equation of motion (3) since no other external force components are considered in this case study. The relevant parameters of the floater are given in Table 1.

To illustrate the effect of the Morison drag force on the dynamics of the floater, TD simulation is performed initially for both cases with and without the drag effect as a comparison. The time-dependent responses are shown and compared in Fig. 4. It can be seen that the motion velocity is clearly overestimated in the case without the drag force, which suggests the importance of implementing it in numerical modeling.

Table 1
Simulation parameters of the case study of Morison drag effect.

Parameters	Quantities
Cylinder radius	5 m
Cylinder height	10 m
Cylinder mass: M_{cy}	402 520 kg
Projected area: A_s	78.5 m^2
Buoy draft	5 m
Water depth	100 m
Drag coefficient: C_d	1
Water density: ρ	1025 kg/m^3

The simulation results obtained from the SL approach are presented in Fig. 5, alongside the results of the corresponding nonlinear TD model and linear FD model for comparison. Specifically, the nonlinear viscous drag force is included in the TD model, as expressed in (38). In contrast,

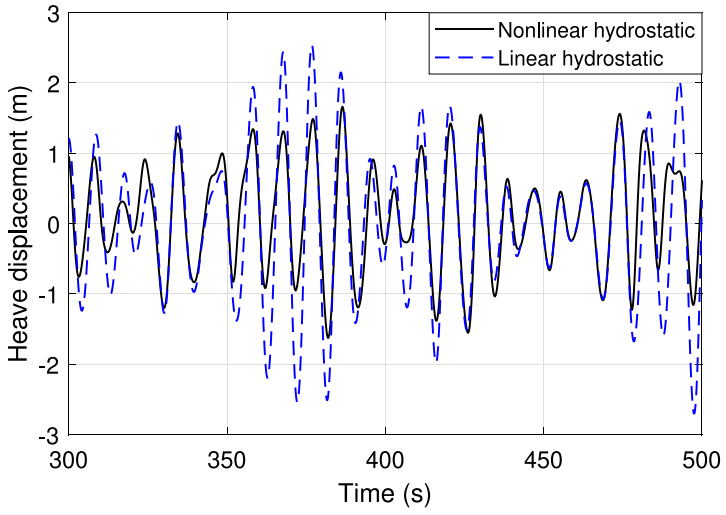

Fig. 12. Instantaneous heave displacement of the spar buoy with considering the linear hydrostatic force and nonlinear hydrostatic force. The simulation conditions are $H_s = 5$ m; $T_p = 10$ s; $B_{vis} = 30$ kNs/m and $K_{mooring} = 50$ kN/m.

the drag effect is omitted in the FD model due to its inherent limitation to fully linear analyses. It is known that a linear constant damping coefficient can be added to represent the viscous drag effect in the linear FD method [36]. However, the accuracy of this approximation is highly sensitive to the selection of the viscous damping constant, which does not align with the inherently nonlinear nature of the Morison drag formulation. To avoid introducing additional sources of uncertainty in the comparison, the viscous drag effect is deliberately excluded in the FD approach here, considering the primary objective here to verifying the extended SL approach.

The results show that the proposed SL approach exhibits good agreement with the nonlinear TD model across a range of peak periods. Even under relatively high sea states, with a significant wave height of 3 m, the relative error of the SL approach compared to the TD model remains below 5%. In comparison, the FD model shows a notable discrepancy relative to the TD model at lower peak periods. In particular, the FD model's relative error reaches approximately 58% at a peak period of 6 s. At higher peak periods, however, all three models present comparable results. This is attributed to the reduced wave velocity at longer periods, where the omission of the wave velocity term has a limited effect on the calculation of the Morison drag force. Conversely, at lower peak periods, wave velocity becomes more significant, leading to greater discrepancies when it is neglected.

4.2. Multi-variate non-differentiable nonlinearity

4.2.1. Uncorrelated variables: PTO force saturation in WECs (case study 2)

This case study is focused on the wave energy conversion. The machinery force saturation in the PTO system of a heaving point absorber WEC is addressed. The schematic of the WEC system is presented in Fig. 6.

The PTO system plays an important role in energy absorption in wave energy conversion [37,38]. It absorbs the kinetic energy of oscillating floater as a form of mechanical energy and then converts the energy to usable electrical power. Due to the randomness of ocean waves, the wave loads can be highly fluctuated even in relatively mild sea states [39,40]. In this sense, PTO systems are commonly equipped with force or torque saturation mechanism to protect themselves from being overloaded and even damaged. The SL method has been adopted to address the single-variate PTO force saturation function, reported in [18], where the PTO mechanism was simplified as a resistive damper and then the PTO force function was only related to the velocity of the WEC's moving floater. Towards a more realistic representation of PTO systems, the reactive control strategy is considered in this work [41]. Then, the description of the PTO force is given as a bi-variate function related to both the displacement and velocity of the floater [42,43]. Considering the saturation mechanism, the PTO force can be expressed as

$$F_{pto}(t) = \begin{cases} R_{pto}v_{wec}(t) + K_{pto}z_{wec}(t), & for \quad |R_{pto}v_{wec}(t) + K_{pto}z_{wec}(t)| \le F_m \\ \text{sign}[R_{pto}v_{wec}(t) + K_{pto}z_{wec}(t)]F_m, & for \quad |R_{pto}v_{wec}(t) + K_{pto}z_{wec}(t)| > F_m \end{cases} \tag{42}$$

where z_{wec} and v_{wec} embody the displacement and velocity of the WEC floater. Given a stationary process, the displacement of the floater and its derivative, namely the velocity, are uncorrelated. This has been mathematically proven in [23]. Thus, the linearization of the multi-variate PTO force saturation falls into the procedure presented in subsection 3.4.2. Referring to (37), the vector of the linearized coefficients for the multi-variate PTO force saturation can therefore be derived as

$$\begin{bmatrix} R_{eq,pto} \\ K_{eq,pto} \end{bmatrix} = \mathbf{E}\left(\begin{bmatrix} \frac{v_{wec}F_{pto}(v_{wec},z_{wec})}{\sigma^2_{v_{wec}}} \\ \frac{z_{wec}F_{pto}(v_{wec},z_{wec})}{\sigma^2_{z_{wec}}} \end{bmatrix} \right) \tag{43}$$

Hence, the statistically linearized PTO force can be expressed as

$$\hat{F}_{pto}(\omega) = R_{eq,pto}\hat{v}_{wec}(\omega) + K_{eq,pto}\hat{z}_{wec}(\omega) \tag{44}$$

where $\hat{v}_{wec}$ and $\hat{z}_{wec}$ are the complex amplitude of the velocity and the displacement of the WEC respectively; $R_{eq,pto}$ and $K_{eq,pto}$ represent the equivalent PTO damping coefficient and the equivalent PTO stiffness coefficient.

Subsequently, incorporating the linearized representation of the nonlinear PTO force into (3) gives the equation of motion of this case:

$$\hat{F}_{e,wec}(\omega) = \hat{z}_{wec}(\omega)\Big\{ -\omega^2\Big[M_{wec} + M_{r,wec}(\omega)\Big] + K_{hs,wec} + K_{eq,pto} + \mathrm{i}\omega\Big[R_{r,wec}(\omega) + R_{eq,pto}\Big]\Big\} \tag{45}$$

where $F_{e,wec}$ stands for the excitation force of the WEC; M_{wec} and $M_{r,wec}$ are the mass and the added mass of the WEC; $K_{hs,wec}$ embodies the linear hydrostatic coefficient of the WEC; and $R_{r,wec}$ denotes the radiation damping of the WEC.

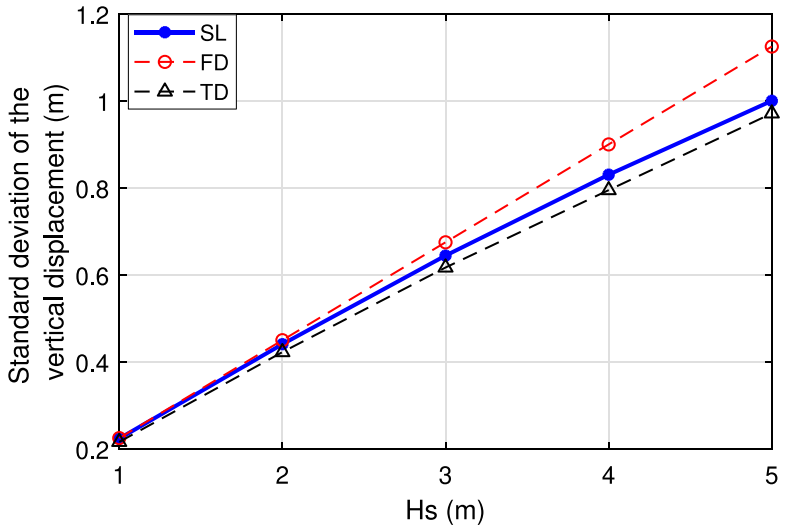

(a) The standard deviation of the vertical displacement of the buoy

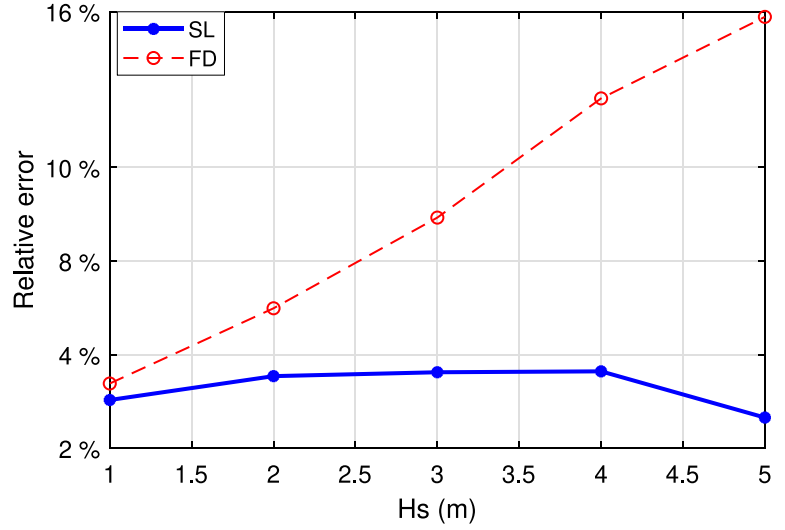

(b) The relative errors of the FD and SL approaches to the TD approach. The mean value of the standard deviation of the displacement across multiple TD simulation runs is used to calculate the relative errors.

Fig. 13. The standard deviation of the displacement of the spar buoy at various significant wave heights, predicted by the linear FD model, the SL approach and the nonlinear TD model. The simulation conditions are $T_p = 10$ s; $B_{vis} = 30$ kNs/m and $K_{mooring} = 50$ kN/m.

As one of the most important performance indicator, the absorbed power of the WEC can be calculated based on the derived solution of the dynamic responses as

$$\overline{P}_{ab} = R_{eq,pto}\sigma^2_{v_{wec}} \tag{46}$$

where $\sigma_{v_{wec}}$ denotes the standard deviation of the velocity of the WEC buoy.

The relevant parameters of the WEC simulated in this case are given in Table 2. The SL approach is applied to evaluate the power absorption of the WEC under various operation conditions, with the corresponding nonlinear TD model and linear FD model implemented for comparison. In the nonlinear TD model, the PTO force saturation is described using the expression (42). Comparatively, a linear representation of the PTO force without the saturation effect is applied in the FD model as

$$\hat{F}_{pto,linear}(\omega) = R_{pto}\hat{v}_{wec}(\omega) + K_{pto}\hat{z}_{wec}(\omega) \tag{47}$$

Table 2
Simulation parameters of the case study of PTO force limit.

Parameters	Quantities
Sphere radius	2.5 m
Sphere draft	2.5 m
Sphere mass: M_{wec}	33 543 kg
Water depth	100 m
Water density: ρ	1025 kg/m^3

For comparison, the PTO power and PTO force are initially computed using the TD model under different PTO force limits, as shown in Figs. 7 and 8. These figures correspond to simulation cases with positive and negative spring stiffness, respectively. It is evident from both figures that the imposed PTO force limit significantly affects the time-dependent profiles of both PTO force and PTO power. The saturation of the PTO force occurs more frequently in cases with a lower

force limit, thereby intensifying the system's nonlinearity. Additionally, it is observed that the instantaneous PTO power tends to be lower when a stricter PTO force limit is applied.

The simulation results of the linear FD, SL and nonlinear TD approaches are presented in Figs. 9 and 10, where various PTO force limits are considered. In Fig. 9, a positive PTO spring stiffness is applied. It is evident that the PTO force limit has a significant impact on the power absorption of the WEC. For instance, when the PTO force limit is defined as 50 kN, the absorbed power estimated by the TD model is around 20 kW. However, the estimated power rises to nearly 28 kW by lifting the PTO force limit to 150 kN. Compared to the TD model, the linear FD model fails to provide a reliable estimation under strict PTO force limits. Specifically, the relative error of the FD model to the TD model even reaches 41% when the PTO force limit is 50 kN. Comparatively, the SL approach demonstrates satisfactory accuracy, with the maximum relative error remaining below 4% across all PTO force limits considered in this case.

The application of reactive PTO control strategies to improve the power production has been emphasized in several studies within the field of WECs [44,45]. However, depending on the specific WEC design, negative PTO spring stiffness is often required to implement such control strategies [46]. To further demonstrate the applicability and robustness of the proposed method for handling multivariate non-differentiable nonlinearities, negative PTO stiffness is considered in this case, and the corresponding simulation results are presented in Fig. 10. By comparing Figs. 10 and 9, it is observed that the power absorbed by the WEC with negative PTO stiffness is higher than that with positive PTO stiffness. For example, the highest absorbed power estimated by the TD model is approximately 43 kW with negative PTO stiffness and, however, 28 kW with positive PTO stiffness. It is acknowledged that this observation is specific to the conditions of this particular case study. Nevertheless, regarding the modeling accuracy, the discrepancy between the FD model and the TD model appears even more notable in the case of negative PTO stiffness. Specifically, at a PTO force limit of 50 kN, the FD model exhibits a relative error as high as 75%, compared to 42% in the case of positive PTO stiffness. Comparatively, the proposed SL approach continues to produce highly accurate results, as shown in Fig. 10, with the maximum relative error remaining below 6%. These results suggest the reliability and robustness of the proposed method in accurately capturing the effects of multivariate non-differentiable nonlinearities in the SL approach.

4.2.2. Correlated variables: Nonlinear hydrostatics of a spar buoy (case study 3)

Floating wind energy has emerged as a main pillar of future marine renewable energy utilization [47,48]. Among a few of the conceptual designs, spar-buoy foundations are widely considered supporting substructure to accommodate floating wind turbines in deep water [49,50]. The nonlinear hydrostatic effect of a spar buoy is addressed in this case study. The schematic of the spar buoy is shown in Fig. 11. The cross-sectional area of the spar buoy is non-uniform, and it can be divided into three regions as rendered in Fig. 11.

Different from the linear hydrostatic representation, the instantaneous variations of the free surface and the wetted surface of the floater are included in the calculation of the nonlinear hydrostatic restoring force. Referring to [22,51], the hydrostatic restoring force can be computed by integrating the static pressure over the floater's wetted surface and minus the gravity force:

$$F_{hs}(t) = -\iint_{S_w(t)} P_{st}\mathbf{n}dS_w - mg \tag{48}$$

where $S_w(t)$ represents the wetted surface, P_{st} denotes the static pressure at a specific point, and $\mathbf{n}$ is the unit normal vector. Based on the Gaussian divergence theorem, (48) can be simplified to:

$$F_{hs}(t) = \rho g V_{sub}(t) - \rho g \Delta z A_{wp}(t) - mg \tag{49}$$

The instantaneous submerged volume V_{sub} and water-plane area A_{wp} depend on the wave elevation η and the buoy's heaving displacement z, while ρ and g represent the water density and gravitational acceleration. The vertical offset Δz between A_{wp} and the reference level $z = 0$ is typically approximated by η. As a result, the hydrostatic restoring force can be formulated in terms of η and z, as given in (50).

$$F_{hs}(z,\eta) = \rho g V_{sub}(z,\eta) - \rho g \eta A_{wp}(z,\eta) - mg \tag{50}$$

Regarding the geometry of the considered spar buoy, the hydrostatic restoring force can be further derived as

$$F_{hs}(z,\eta) = \begin{cases} \rho g\left[\pi\left(\frac{D_2}{2}\right)^2 H_2 + \frac{\pi H_1}{3}\left(\left(\frac{D_2}{2}\right)^2 + \left(\frac{D_1}{2}\right)^2 + \frac{D_2}{2}\frac{D_1}{2}\right)\right. \\ \left. +\pi\left(\frac{D_1}{2}\right)^2\left(\eta - z - \frac{H_1}{2}\right)\right] \\ -\rho g\eta\left[\pi\left(\frac{D_1}{2}\right)^2\right] - mg, (\eta - z) \in \text{Region 1} \\ \rho g\left[\pi\left(\frac{D_2}{2}\right)^2 H_2 + \frac{\pi\left[\frac{H_1}{2}+(\eta-z)\right]}{3}\left(\left(\frac{D_2}{2}\right)^2\right.\right. \\ \left. + \left(\frac{D_2}{2} - \frac{\frac{H_1}{2}+(\eta-z)}{H_1}\frac{D_2-D_1}{2}\right)^2\right. \\ \left.\left. + \frac{D_2}{2}\frac{\frac{H_1}{2}+(\eta-z)}{H_1}\frac{D_2-D_1}{2}\right)\right] \\ -\rho g\eta\left[\pi\left(\frac{\frac{H_1}{2}+(\eta-z)}{H_1}\frac{D_2-D_1}{2}\right)^2\right] - mg, \ (\eta - z) \in \text{Region 2} \\ \rho g\left[\pi\left(\frac{D_2}{2}\right)^2 (H_2 + (\eta - z))\right] \quad - \rho g\eta\left[\pi(\frac{D_2}{2})^2\right] \\ -mg, \ (\eta - z) \in \text{Region 3} \end{cases} \tag{51}$$

It can be deduced that (51) is not differentiable at the intersection point between every two regions of the buoy geometry as depicted in Fig. 11. Additionally, as the wave elevation is inherently correlated to the buoy's motion, the vector of the linearized coefficients can be derived referring to (37) as

$$\begin{bmatrix} K_{eq,\eta} \\ K_{eq,z} \end{bmatrix} = \begin{bmatrix} \sigma_\eta^2 & \sigma_{\eta z} \\ \sigma_{z\eta} & \sigma_z^2 \end{bmatrix}^{-1} \mathbf{E}\left(\begin{bmatrix} \eta F_{hs}(\eta, z) \\ z F_{hs}(\eta, z) \end{bmatrix}\right) \tag{52}$$

Therefore, the linearized hydrostatic restoring force in the spectral domain can be derived as

$$\hat{F}_{hs} = K_{eq,\eta}\hat{\eta}(\omega) + K_{eq,z}\hat{z}(\omega) \tag{53}$$

where $K_{eq,\eta}$ and $K_{eq,z}$ are the linearized equivalent hydrostatic stiffness coefficients related to the wave elevation and the displacement of the spar buoy.

It is assumed that the buoy is connected to mooring lines with pretension and only the heave motion is considered in this case. The mooring effect can therefore be modeled as a linear spring. In this sense, the equation of motion can be given as

$$\hat{F}_{e,s}(\omega) + K_{eq,\eta}\hat{\eta}(\omega) = \hat{z}(\omega)\Big\{-\omega^2\big(M_s + M_{r,s}(\omega)\big) + K_{mooring} - K_{eq,z} + \mathrm{i}\omega\big(R_{r,s}(\omega) + R_{vis}\big)\Big\} \tag{54}$$

where $F_{e,s}$ stands for the excitation force of the spar buoy; M_s and $M_{r,s}$ are the mass and the added mass of the spar buoy; and $R_{r,s}$ denotes the radiation damping of the spar buoy. where $K_{mooring}$ and R_{vis} denote the mooring stiffness and the viscous damping. They are assumed to be constant coefficients in this case since the focus of this case study is located on the nonlinear hydrostatic effect.

The specification of the spar buoy dimension and relevant simulation parameters are provided in Table 3. In this case, the nonlinear TD model employs the complete expression (51) to include the nonlinear hydrostatic force. While a linear hydrostatic stiffness coefficient is used

Table 3
Simulation parameters of the case study of hydrostatics of the spar buoy.

Parameters	Quantities
Diameter of Region 1: D_1	4 m
Diameter of Region 2: D_2	8 m
Diameter of mean water plane: D_{mean}	6 m
Height of Region 2: H_1	4 m
Height of Region 3: H_2	8 m
Buoy mass: M_s	487 900 kg
Water density ρ	1025 kg/m^3
Water depth	200 m
Constant vicious drag damping: R_{vis}	30 kNs/m
Mooring line tension in heave: $K_{mooring}$	50 kN/m

Table 4
Computational time of different numerical modeling approaches for one simulation case.

Case studies	Numerical methods	Computational time
Case study 1	FD	1.9×10^{-2} s
(T_p = 10 s)	TD	123.5 s (30-runs)
	SL	3.9×10^{-1} s
Case study 2	FD	4.1×10^{-2} s
(PTO force limit of 90 kN,	TD	155.2 s (30-runs)
positive PTO stiffness)	SL	2.8×10^{-1} s
Case study 3	FD	3.9×10^{-2} s
(H_S = 3 m)	TD	161.7 s (30-runs)
	SL	4.9×10^{-1} s

in the FD model, given as

$$F_{hs,linear} = -\rho g \pi (\frac{D_{mean}}{2})^2 \quad (55)$$

where D_{mean} is the diameter of the water-plane area of the spar buoy at the still water level.

To illustrate the difference, TD simulations are conducted for the spar buoy using both linear and nonlinear representations of the hydrostatic force. The resulting instantaneous displacement of the spar buoy is shown in Fig. 12. It is observed that the linear hydrostatic representation generally results in significantly higher displacement values compared to the nonlinear case. This implies the importance of incorporating the nonlinear hydrostatic force for a more realistic estimation of the system response.

The simulation results obtained by the linear FD modeling, nonlinear TD modeling and the SL approaches are presented in Fig. 13, where the standard deviation of the vertical displacement of the spar buoy is estimated under varying significant wave heights. At relatively low significant wave heights, the FD, SL, and TD approaches produce similar results. However, as the significant wave height increases, the accuracy of the FD model declines, with a relative error exceeding 10% compared to the TD model when the significant wave height surpasses 3.5 m. This discrepancy arises from the amplification of the nonlinear hydrostatic effect at higher wave heights, which leads to larger motions and wave elevations. In contrast, the proposed SL approach maintains high accuracy across all considered conditions, with the relative error consistently remaining below 4%, even at larger significant wave heights.

4.3. Identification of computational efficiency

The most significant advantage of the SL approach is its high computational efficiency while accounting for nonlinear effects. The computational time required to complete a single simulation using different numerical modeling approaches is presented in Table 4. All simulations are performed on the same machine, equipped with an Intel i7/2.80 GHz processor. For a fair comparison, the simulation conditions are kept identical and are specified in the table. It is important to note that the total computational time reported for the TD model accounts for 30 simulation runs, as the TD model must be repeated multiple times in each case to average the results and reduce random errors [7].

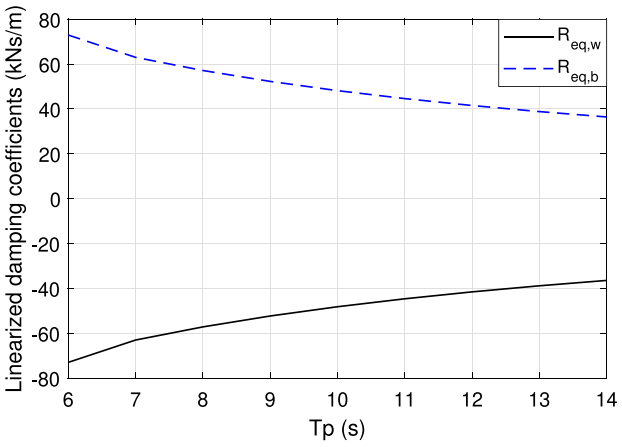

Fig. A.14. Linearized damping coefficients utilized in case study 1, H_s = 3.0 m.

As shown in Table 4, the SL approach requires approximately 10–20 times more computational effort than the FD model. However, the computational time of the SL approach remains three orders of magnitude lower than that of the TD model. This suggests the significant advantage of applying the SL approach to scenarios where a large number of simulations are in demand, such as early-stage design iterations, systematic optimizations, and large-scale configuration planning of marine renewable energy plants. Furthermore, the SL approach could also significantly accelerate the control design and control parameter optimizations of floating renewable energy devices, such as WECs.

5. Conclusion

This study has described the methodology and demonstrated the applicability of the SL method for incorporating multivariate non-differentiable nonlinear effects, focusing on the typical complex nonlinearities encountered in floating renewable energy devices. To address the challenges posed by the non-differentiability of multivariate nonlinear functions, the existing SL method has been further developed. The mathematical derivation for handling multivariate non-differentiable nonlinearities is presented in detail.

Three case studies, representing various applications in floating renewable energy systems, have been conducted in this work. These case studies address multivariate differentiable nonlinearities, multivariate non-differentiable nonlinearities involving uncorrelated variables, and multivariate non-differentiable nonlinearities involving correlated variables, respectively. The accuracy of the extended SL method was verified against the higher-fidelity nonlinear TD model across these cases. The results show that, despite the complexity of the nonlinear effects considered, the extended SL method maintained relative errors below 6%, while achieving computational times only slightly higher than the FD model and several orders of magnitude faster than the TD model. The primary source of errors of the SL method arises from the Gaussian assumption of the system, which has been demonstrated in [12]. Comparatively, the FD model exhibited relative errors exceeding 70% in certain cases.

These findings confirm that the SL approach provides an effective balance between accuracy and computational efficiency. Moreover, the limitations previously associated with applying the SL method to

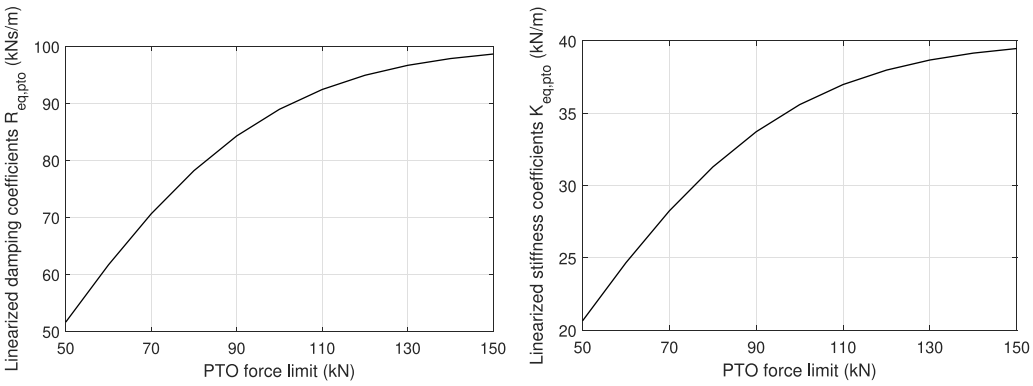

(a) Linearized damping coefficients. (b) Linearized stiffness coefficients.

Fig. B.15. The linearized coefficients utilized in case study 2. The simulation conditions are $H_s = 4$ m; $T_p = 10$ s; $B_{pto} = 100$ kNs/m and $K_{pto} = 40$ kN/m.

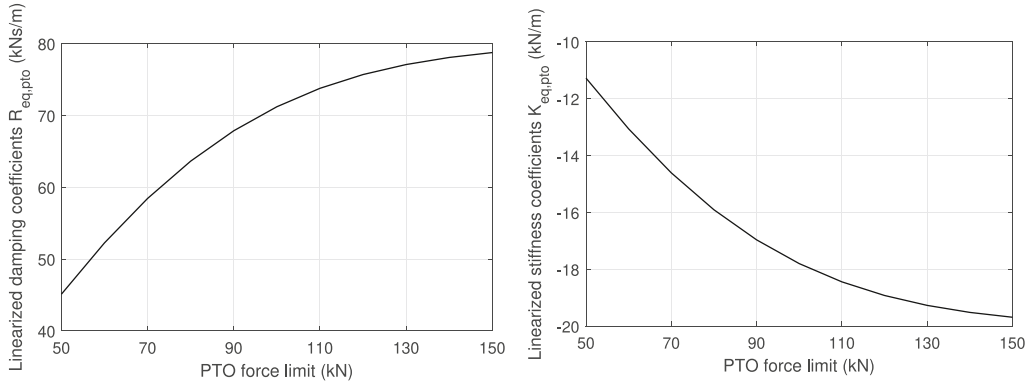

(a) Linearized damping coefficients. (b) Linearized stiffness coefficients.

Fig. B.16. The linearized coefficients utilized in case study 2. The simulation conditions are $H_s = 4$ m; $T_p = 10$ s; $B_{pto} = 80$ kNs/m and $K_{pto} = -20$ kN/m.

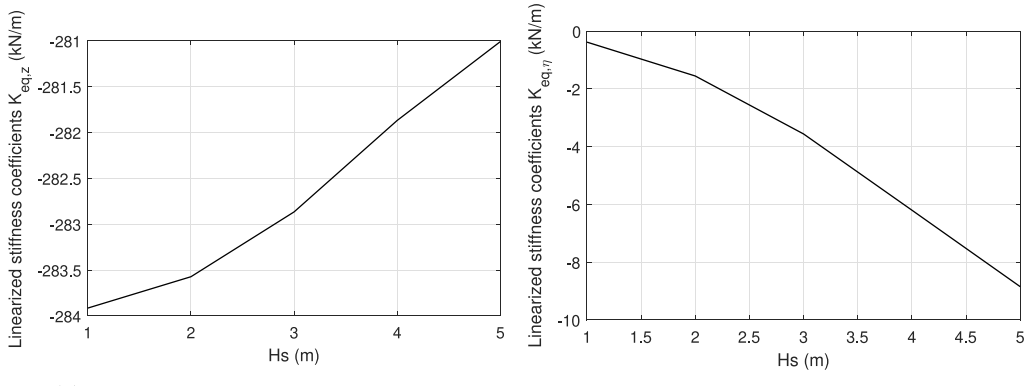

(a) Linearized stiffness coefficients $K_{eq,z}$. (b) Linearized stiffness coefficients $K_{eq,\eta}$.

Fig. C.17. The linearized coefficients utilized in case study 3. The simulation conditions are $T_p = 10$ s; $B_{vis} = 30$ kNs/m and $K_{mooring} = 50$ kN/m.

complex nonlinearities in floating renewable energy systems have been successfully lifted.

CRediT authorship contribution statement

Jian Tan: Writing – original draft, Supervision, Methodology, Data curation, Writing – review & editing, Validation, Resources, Formal analysis, Conceptualization, Visualization, Software, Investigation. **Lei Zuo:** Validation, Writing – review & editing, Supervision, Investigation, Visualization, Methodology, Formal analysis. **George Lavidas:** Supervision, Validation, Methodology, Formal analysis, Writing – review & editing, Project administration, Investigation, Funding acquisition. **Andrei Metrikine:** Visualization, Software, Investigation, Conceptualization, Supervision, Project administration, Funding acquisition, Writing – review & editing, Validation, Resources, Methodology, Formal analysis.

Declaration of competing interest

The authors declare that they have no known competing financial interests or personal relationships that could have appeared to influence the work reported in this paper.

Appendix A. Derived linearized coefficients in case study 1

See Fig. A.14.

Appendix B. Derived linearized coefficients in case study 2

See Figs. B.15 and B.16.

Appendix C. Derived linearized coefficients in case study 3

See Fig. C.17.

References

[1] D. Magagna, A. Uihlein, Ocean energy development in europe: Current status and future perspectives, Int. J. Mar. Energy 11 (2015) 84–104.
[2] M.L. Martínez, V. Chávez, V. De la Cruz, O. Pérez-Maqueo, A. Wojtarowski, R. Silva, Ocean energy, in: The Palgrave Handbook of Global Sustainability, Springer, 2023, pp. 177–192.
[3] M. Quirapas, A. Taeihagh, Ocean renewable energy development in southeast Asia: Opportunities, risks and unintended consequences, Renew. Sustain. Energy Rev. 137 (2021) 110403.
[4] H. Díaz, J. Serna, J. Nieto, C. Guedes Soares, Market needs, opportunities and barriers for the floating wind industry, J. Mar. Sci. Eng. 10 (7) (2022) 934.
[5] S. Bashetty, S. Ozcelik, Review on dynamics of offshore floating wind turbine platforms, Energies 14 (19) (2021) 6026.
[6] B. Guo, J.V. Ringwood, A review of wave energy technology from a research and commercial perspective, IET Renew. Power Gener. 15 (14) (2021) 3065–3090.
[7] Numerical Modelling of Wave Energy Converters, Numerical Modelling of Wave Energy Converters, 2016.
[8] E. Ransley, D. Greaves, A. Raby, D. Simmonds, M. Hann, Survivability of wave energy converters using CFD, Renew. Energy 109 (2017) 235–247.
[9] W. Cummins, W. Iiuhl, A. Uinm, The impulse response function and ship motions, 1962.
[10] J. Pastor, Y. Liu, Frequency and time domain modeling and power output for a heaving point absorber wave energy converter, Int. J. Energy Environ. Eng. 5 (2–3) (2014) 1–13.
[11] M. Lawson, Y.-H. Yu, K. Ruehl, C. Michelen, et al., Development and demonstration of the WEC-sim wave energy converter simulation tool, 2014.
[12] M. Folley, T. Whittaker, Spectral modelling of wave energy converters, Coast. Eng. 57 (10) (2010) 892–897.
[13] M. Folley, T. Whittaker, Validating a spectral-domain model of an OWC using physical model data, Int. J. Mar. Energy 2 (2013) 1–11.
[14] L.S.P.d. Silva, Nonlinear stochastic analysis of wave energy converters via statistical linearization, Master's thesis, Universidade de São Paulo, 2019.
[15] P.D. Spanos, F.M. Strati, G. Malara, F. Arena, An approach for non-linear stochastic analysis of U-shaped OWC wave energy converters, Probabilistic Eng. Mech. 54 (2018) 44–52.
[16] L. Silva, N. Sergiienko, C. Pesce, B. Ding, B. Cazzolato, H. Morishita, Stochastic analysis of nonlinear wave energy converters via statistical linearization, Appl. Ocean Res. 95 (2020) 102023.
[17] L.S. da Silva, B.S. Cazzolato, N.Y. Sergiienko, B. Ding, H.M. Morishita, C.P. Pesce, Statistical linearization of the morison's equation applied to wave energy converters, J. Ocean. Eng. Mar. Energy 6 (2020) 157–169.
[18] J. Tan, H. Polinder, A.J. Laguna, S. Miedema, The application of the spectral domain modeling to the power take-off sizing of heaving wave energy converters, Appl. Ocean Res. 122 (2022) 103110.
[19] J. Tan, W. Tao, A.J. Laguna, H. Polinder, Y. Xing, S. Miedema, A spectral-domain wave-to-wire model of wave energy converters, Appl. Ocean Res. 138 (2023) 103650.
[20] J. Tan, A.J. Laguna, Spectral-domain modelling of wave energy converters as an efficient tool for adjustment of PTO model parameters, in: Proceedings of the European Wave and Tidal Energy Conference, vol. 15, 2023.
[21] M. Bonfanti, N. Faedo, G. Mattiazzo, Towards efficient control synthesis for nonlinear wave energy conversion systems: impedance-matching meets the spectral-domain, Nonlinear Dynam. 112 (13) (2024) 11085–11109.
[22] J. Tan, G. Lavidas, A modified spectral-domain model for nonlinear hydrostatic restoring force of heaving wave energy converters, Ocean Eng. 309 (2024) 118581.
[23] J.B. Roberts, P.D. Spanos, Random vibration and statistical linearization, Courier Corporation, 2003.
[24] M. Bonfanti, S.A. Sirigu, Spectral-domain modelling of a non-linear wave energy converter: Analytical derivation and computational experiments, Mech. Syst. Signal Process. 198 (2023) 110398.
[25] W. Shi, C. Yan, Z. Ren, Z. Yuan, Y. Liu, S. Zheng, X. Li, X. Han, Review on the development of marine floating photovoltaic systems, Ocean Eng. 286 (2023) 115560.
[26] A. Pecher, Handbook of Ocean Wave Energy, vol. 7, 2017.
[27] S. Brahma, H.R. Ossareh, Stochastic linearization of multivariate nonlinearities, 2018, arXiv preprint arXiv:1807.06135.
[28] D. Micallef, A. Rezaeiha, Floating offshore wind turbine aerodynamics: Trends and future challenges, Renew. Sustain. Energy Rev. 152 (2021) 111696.
[29] S.-E. Abdelmoteleb, E.E. Bachynski-Polić, A frequency-domain optimization procedure for catenary and semi-taut mooring systems of floating wind turbines, Mar. Struct. 101 (2025) 103768.
[30] L.S.P. Da Silva, M. de Oliveira, B. Cazzolato, N. Sergiienko, G. Amaral, B. Ding, Statistical linearisation of a nonlinear floating offshore wind turbine under random waves and winds, Ocean Eng. 261 (2022) 112033.
[31] M. Penalba, T. Kelly, J. Ringwood, Using NEMOH for Modelling Wave Energy Converters : A Comparative Study with WAMIT, in: 12th European Wave and Tidal Energy Conference, 2017, p. 10.
[32] J.M.J. Journée, W.W. Massie, R.H.M. Huijsmans, Offshore hydrodynamics, 2015.
[33] T. Pérez, T. Fossen, Time-vs. frequency-domain identification of parametric radiation force models for marine structures at zero speed, Model. Identif. Control 29 (1) (2008) 1–19.
[34] J. Palm, C. Eskilsson, L. Bergdahl, R. Bensow, Assessment of Scale Effects, Viscous Forces and Induced Drag on a Point-Absorbing Wave Energy Converter by CFD Simulations, J. Mar. Sci. Eng. 6 (4) (2018) 124.
[35] Y. Ren, V. Venugopal, W. Shi, Dynamic analysis of a multi-column TLP floating offshore wind turbine with tendon failure scenarios, Ocean Eng. 245 (2022) 110472.
[36] C. Liang, L. Zuo, On the dynamics and design of a two-body wave energy converter, Renew. Energy 101 (2017) 265–274.
[37] M. Prado, H. Polinder, Direct drive wave energy conversion systems: An introduction, Electrical Drives for Direct Drive Renewable Energy Systems, Woodhead Publishing Limited, 2013, pp. 175–194.
[38] R. So, A. Simmons, T. Brekken, K. Ruehl, C. Michelen, Development of PTO-SIM: A power performance module for the open-source wave energy converter code WEC-Sim, Proc. Int. Conf. Offshore Mech. Arct. Eng. - OMAE 9 (May) (2015).
[39] J. Tan, X. Wang, H. Polinder, A.J. Laguna, S.A. Miedema, Downsizing the Linear PM Generator in Wave Energy Conversion for Improved Economic Feasibility, J. Mar. Sci. Eng. 10 (9) (2022).
[40] A. Babarit, J. Hals, M.J. Muliawan, A. Kurniawan, T. Moan, J. Krokstad, Numerical benchmarking study of a selection of wave energy converters, Renew. Energy 41 (2012) 44–63.
[41] J. Hals, T. Bjarte-Larsson, J. Falnes, Optimum Reactive Control and Control by Latching of a Wave-Absorbing Semisubmerged Heaving Sphere, 21st Int. Conf. Offshore Mech. Arct. Eng. (January) (2002) 415–423.
[42] S. Zou, O. Abdelkhalik, R. Robinett, G. Bacelli, D. Wilson, Optimal control of wave energy converters, Renew. Energy 103 (2) (2017) 217–225.
[43] J.V. Ringwood, Wave energy control: Status and perspectives 2020, IFAC- Pap. 53 (2) (2020) 12271–12282.
[44] J. Tan, H. Polinder, A.J. Laguna, P. Wellens, S.A. Miedema, The influence of sizing of wave energy converters on the techno-economic performance, J. Mar. Sci. Eng. 9 (1) (2021) 52.
[45] J. Hals, J. Falnes, T. Moan, A comparison of selected strategies for adaptive control of wave energy converters, 2011.
[46] C.A.M. Ströfer, D.T. Gaebele, R.G. Coe, G. Bacelli, Control co-design of power take-off systems for wave energy converters using WecOptTool, IEEE Trans. Sustain. Energy 14 (4) (2023) 2157–2167.
[47] B. Zhou, Z. Zhang, G. Li, D. Yang, M. Santos, Review of key technologies for offshore floating wind power generation, Energies 16 (2) (2023) 710.
[48] J. McMorland, M. Collu, D. McMillan, J. Carroll, Operation and maintenance for floating wind turbines: A review, Renew. Sustain. Energy Rev. 163 (2022) 112499.
[49] S.Y. Zhang, G. Tan, Y. Deng, Y. Zhang, Y. Wang, Z. Wang, Vibration mitigation of spar-buoy floating wind turbines using a nonlinear energy sink, Ocean Eng. 304 (2024) 117883.
[50] M. Barooni, T. Ashuri, D. Velioglu Sogut, S. Wood, S. Ghaderpour Taleghani, Floating offshore wind turbines: Current status and future prospects, Energies 16 (1) (2022) 2.
[51] G. Giorgi, J.V. Ringwood, Nonlinear Froude-Krylov and viscous drag representations for wave energy converters in the computation/fidelity continuum, Ocean Eng. 141 (2017) 164–175.